Water Resources Research

RESEARCH ARTICLE

Key Points:
- New computational approach to coupled multiphase flow and geomechanics
- Faults are represented as surfaces, capable of simulating runaway slip
- Unconditionally stable sequential solution of the fully coupled equations

Supporting Information:
- Readme
- Videos S1 and S2

Correspondence to:
R. Juanes,
juanes@mit.edu

Coupled multiphase flow and poromechanics: A computational model of pore pressure effects on fault slip and earthquake triggering

Birendra Jha[1] and Ruben Juanes[1]

[1]Department of Civil and Environmental Engineering, Massachusetts Institute of Technology, Cambridge, Massachusetts, USA

Abstract The coupling between subsurface flow and geomechanical deformation is critical in the assessment of the environmental impacts of groundwater use, underground liquid waste disposal, geologic storage of carbon dioxide, and exploitation of shale gas reserves. In particular, seismicity induced by fluid injection and withdrawal has emerged as a central element of the scientific discussion around subsurface technologies that tap into water and energy resources. Here we present a new computational approach to model coupled multiphase flow and geomechanics of faulted reservoirs. We represent faults as surfaces embedded in a three-dimensional medium by using zero-thickness interface elements to accurately model fault slip under dynamically evolving fluid pressure and fault strength. We incorporate the effect of fluid pressures from multiphase flow in the mechanical stability of faults and employ a rigorous formulation of nonlinear multiphase geomechanics that is capable of handling strong capillary effects. We develop a numerical simulation tool by coupling a multiphase flow simulator with a mechanics simulator, using the unconditionally stable fixed-stress scheme for the sequential solution of two-way coupling between flow and geomechanics. We validate our modeling approach using several synthetic, but realistic, test cases that illustrate the onset and evolution of earthquakes from fluid injection and withdrawal.

1. Introduction

Coupling between fluid flow and mechanical deformation in porous media plays a critical role in subsurface hydrology, hydrocarbon recovery, and seismic activity in the Earth's crust. Subsidence due to groundwater withdrawal has been studied for decades, but continues to pose significant challenges in many parts of the world [*Geertsma*, 1973; *Gambolati and Freeze*, 1973; *Bear and Corapcioglu*, 1981; *Mossop and Segall*, 1997; *Galloway et al.*, 1998; *Gambolati et al.*, 2000; *Galloway and Burbey*, 2011]. Production and injection of fluids in oil, gas, and geothermal fields have also been associated with surface subsidence and earthquakes along preexisting faults [*Raleigh et al.*, 1976; *Yerkes and Castle*, 1976; *Lofgren*, 1981; *Segall*, 1989; *Fialko and Simons*, 2000; *Ellsworth*, 2013; *Brodsky and Lajoie*, 2013]. Earthquakes triggered due to groundwater withdrawal [*Gonzalez et al.*, 2012], reservoir impoundment [*Carder*, 1945; *Lomnitz*, 1974; *Gupta*, 2002], and wastewater disposal [*Keranen et al.*, 2013; *van der Elst et al.*, 2013] have been reported as has been fluctuation in groundwater levels due to earthquakes [*Roeloffs*, 1996; *Wang et al.*, 2001].

Recently, coupled flow and geomechanics has also gained attention due to its role in the long-term geologic storage of carbon dioxide CO_2 in saline aquifers, which is widely regarded as a promising technology to help mitigate climate change by significantly reducing anthropogenic CO_2 emissions into the atmosphere [e.g., *Lackner*, 2003; *Pacala and Socolow*, 2004; *IPCC*, 2005; *Orr*, 2009; *Szulczewski et al.*, 2012]. Injection of CO_2 requires displacement or compression of the ambient groundwater, and an overpressurization of the target aquifer, which could fracture the caprock [*Birkholzer and Zhou*, 2009], trigger seismicity, and cause shear slip on preexisting faults [*Rutqvist et al.*, 2007, 2008; *Chiaramonte et al.*, 2008; *Rutqvist et al.*, 2010; *Morris et al.*, 2011a, 2011b; *Cappa and Rutqvist*, 2011a, 2011b], and potentially compromise the caprock by activating faults [*Zoback and Gorelick*, 2012a].

A similar set of issues arises in the extraction of oil and natural gas from low-permeability hydrocarbon reservoirs, and in particular oil and gas shales. The extraction of shale gas has undergone a revolution due to the massive deployment of a technology called hydraulic fracturing, or "fracking" [*Cueto-Felgueroso and Juanes*, 2013]. Concerns have been raised regarding whether fracking—and, in particular, subsurface

disposal of produced water—may lead to venting of methane from gas shales [*Howarth et al.*, 2011] or to contamination of groundwater by fracking fluids [*Osborn et al.*, 2011; *Jackson et al.*, 2013]. Therefore, understanding of the potential leakage through faults undergoing slip from injection overpressure has become a key point of the scientific discussion surrounding the viability of CCS as a climate change mitigation technology [*Zoback and Gorelick*, 2012a; *Juanes et al.*, 2012; *Zoback and Gorelick*, 2012b] and the risks associated with the production of shale gas [*Warner et al.*, 2012a; *Engelder*, 2012; *Warner et al.*, 2012b].

Despite the growing environmental, industrial, and economic importance of coupled flow and geomechanics, many aspects remain poorly understood. One of the fundamental unresolved issues is the ability to describe the mechanical and hydraulic behavior of faults, and the influence of the full stress tensor and change in pressure on fault slip. Injection and production of fluids from a geologic reservoir induce changes in the state of stress, both within and outside the reservoir, and these can affect the stability of preexisting faults. The effects of injection and production depend on the initial state of stress, the elastic moduli of the geologic structures, and the fault frictional properties. The effects are not always intuitively obvious and should be quantified using geomechanical models. This requires the development of a new generation of geomechanical models that include coupling between fluid flow and fault motion.

Currently, geomechanical models typically treat faults as failure zones that are discretized as three-dimensional elements where the rheology is allowed to be different (e.g., plastic with weakening failure) than in the rest of the domain (e.g., elastoplastic with hardening law) [*Rutqvist et al.*, 2008; *Cappa and Rutqvist*, 2011a, 2011b]. This approach has several limitations, including the inability to model actual slip along a surface of discontinuity, and the dependence of the simulation results on the level of grid refinement. Other models represent faults as surfaces using interface elements [e.g., *Ferronato et al.*, 2008], but so far these models are uncoupled to flow, and they model fault slip using a penalty method [*Glowinsky and Le Tallec*, 1989]. Such methods require a priori selection of the penalty parameters for the fault, and therefore cannot represent dynamically evolving fault strength, such as slip-weakening or rate- and state-friction models [*Dieterich*, 1979]. Interface elements have also been used to model tensile fractures during the simulation of coupled flow and deformation in fractured media [*Segura and Carol*, 2004, 2008a, 2008b].

The interactions between flow and geomechanics have been modeled computationally using various coupling schemes [*Dean et al.*, 2006; *Jeannin et al.*, 2007; *Jha and Juanes*, 2007; *Mainguy and Longuemare*, 2002; *Minkoff et al.*, 2003; *Settari and Mourits*, 1998; *Settari and Walters*, 2001; *Thomas et al.*, 2003; *Tran et al.*, 2004, 2005; *Kim et al.*, 2011a, 2011b, 2011c, 2013]. In the fully implicit method, one solves the coupled discrete nonlinear system of equations simultaneously, typically using the Newton-Raphson scheme [*Sukirman and Lewis*, 1993; *Pao and Lewis*, 2002; *Lewis et al.*, 2003; *Li et al.*, 2005; *Ferronato et al.*, 2010]. The fully implicit method guarantees unconditional stability if the mathematical problem is well posed, but the simulation of flow and geomechanics for realistic fields becomes computationally very expensive [*Settari and Mourits*, 1998; *Thomas et al.*, 2003; *Jha and Juanes*, 2007]. Sequential approaches to modeling coupled flow and geomechanics are highly desirable because they offer the flexibility of using separate simulators for each subproblem [*Felippa and Park*, 1980; *Samier and Gennaro*, 2007; *Minkoff et al.*, 2003; *Rutqvist et al.*, 2002]. The design and analysis of sequential methods with appropriate stability properties for poromechanics and thermomechanics has a long history [*Zienkiewicz et al.*, 1988; *Armero and Simo*, 1992, 1993; *Armero*, 1999; *Settari and Mourits*, 1998; *Mainguy and Longuemare*, 2002; *Jeannin et al.*, 2007]. Recently, a new sequential method for coupled flow and geomechanics, termed the "fixed-stress split," has been proposed and analyzed [*Kim et al.*, 2011a, 2011b, 2013]. Stability and convergence analyses have shown that the fixed-stress split inherits the dissipation properties of the continuum problem and is therefore unconditionally stable, both in the linear (poroelastic) and nonlinear (poroelastoplastic) regime. The analysis has shown that the fixed-stress split enjoys excellent convergence properties, even in the quasi-incompressible limit. It has also been shown recently that the stability and convergence properties of the fixed-stress split for single-phase flow carry over to multiphase systems if a proper definition of pore pressure, the "equivalent pore pressure" [*Coussy*, 2004], is used [*Kim et al.*, 2013].

In this article, we present a new computational model for coupled flow and geomechanics of faulted reservoirs. We couple a flow simulator with a mechanics simulator using the fixed-stress scheme [*Kim et al.*, 2011b]. We employ a rigorous formulation of nonlinear multiphase geomechanics [*Coussy*, 1995] based on the increment in mass of fluid phases, instead of the more common, but less accurate, scheme based on the change in porosity [*Settari and Mourits*, 1998; *Minkoff et al.*, 2003; *Thomas et al.*, 2003; *Tran et al.*, 2004, 2005; *Rutqvist*

et al., 2002]. Our nonlinear formulation is required to properly model systems with high compressibility or strong capillary [*Coussy*, 1995], as can be the case for geologic CO_2 sequestration [*Rutqvist et al.*, 2007, 2008], groundwater extraction from unconfined aquifers [*Gambolati and Freeze*, 1973; *Gonzalez et al.*, 2012], and shale gas production [*Engelder*, 2012]. To account for the effect of surface stresses along fluid-fluid interfaces, we use the equivalent pore pressure in the definition of multiphase effective stress [*Coussy*, 2004; *Kim et al.*, 2013]. We model faults as surfaces of discontinuity using interface elements [*Aagaard et al.*, 2012, 2013]. This allows us to model stick-slip behavior on the fault surface for dynamically evolving fault strength.

2. Governing Equations

2.1. Balance Laws

We use a classical continuum representation in which the fluids and the solid skeleton are viewed as overlapping continua [*Bear*, 1972; *Coussy*, 2005]. The governing equations for coupled flow and geomechanics are obtained from conservation of mass and balance of linear momentum. We assume that the deformations are small, that the geomaterial is isotropic, and that the conditions are isothermal. Let Ω be our domain of interest and $\partial\Omega$ be its closed boundary. Under the quasi-static assumption for earth displacements, the governing equation for linear momentum balance of the solid/fluid system can be expressed as

$$\nabla \cdot \boldsymbol{\sigma} + \rho_b \boldsymbol{g} = \boldsymbol{0}, \tag{1}$$

where $\boldsymbol{\sigma}$ is the Cauchy total stress tensor, $\boldsymbol{g}$ is the gravity vector, and $\rho_b = \phi \sum_{\beta}^{n_{\text{phase}}} \rho_\beta S_\beta + (1 - \phi)\rho_s$, is the bulk density, ρ_β and S_β are the density and saturation of fluid phase β, ρ_s is the density of the solid phase, ϕ is the true porosity, and n_{phase} is the number of fluid phases. The true porosity is defined as the ratio of the pore volume V_p to the bulk volume V_b in the current (deformed) configuration. Assuming that the fluids are immiscible, the mass conservation equation for each phase α is

$$\frac{dm_\alpha}{dt} + \nabla \cdot \boldsymbol{w}_\alpha = \rho_\alpha f_\alpha, \tag{2}$$

where the accumulation term dm_α/dt describes the time variation of fluid mass relative to the motion of the solid skeleton, $\boldsymbol{w}_\alpha$ is the mass flux of fluid phase α relative to the solid skeleton, and f_α is the volumetric source term for phase α. Balance equations (1) and (2) are coupled by virtue of poromechanics. On one hand, changes in the pore fluid pressure lead to changes in effective stress and induce deformation of the porous material—such as ground subsidence caused by groundwater withdrawal. On the other hand, deformation of the porous medium affects fluid mass content and fluid pressure. The simplest model of this two-way coupling is Biot's macroscopic theory of poroelasticity [*Biot*, 1941; *Geertsma*, 1957; *Coussy*, 1995]. In the remainder of this section, we provide the mathematical description of poroelasticity, first for single-phase, and then for multiphase fluid systems.

2.2. Single-Phase Poromechanics

For isothermal single-phase flow of a slightly compressible fluid in a poroelastic medium with no stress dependence of permeability, the single-phase fluid mass conservation equation reduces to

$$\frac{dm}{dt} + \nabla \cdot \boldsymbol{w} = \rho_f f, \tag{3}$$

where m is the fluid mass content (fluid mass per unit bulk volume of porous medium), ρ_f is the fluid density, $\boldsymbol{w} = \rho_f \boldsymbol{v}$ is the fluid mass flux (fluid mass flow rate per unit area and time), and $\boldsymbol{v}$ is the seepage velocity relative to the deforming skeleton, given by Darcy's law:

$$\boldsymbol{v} = -\frac{\boldsymbol{k}}{\mu}(\nabla p - \rho_f \boldsymbol{g}), \tag{4}$$

where $\boldsymbol{k}$ is the intrinsic permeability tensor, μ is the fluid dynamic viscosity, and p is the pore fluid pressure [*Bear*, 1972]. It is useful to define the fluid content variation ζ

$$\zeta := \frac{\delta m}{\rho_{f,0}}, \tag{5}$$

where $\delta m = m - m_0$ is the increment in fluid mass content with respect to the initial reference state and $\rho_{f,0}$ is the reference fluid density.

The self-consistent theory of poroelastic behavior proposed by *Biot* [1941] links the changes in total stress and fluid pressure with changes in strain and fluid content. Following *Coussy* [1995], the poroelasticity equations can be written in incremental form as

$$\delta\boldsymbol{\sigma} = \mathbf{C}_{dr} : \boldsymbol{\varepsilon} - b\delta p\mathbf{1}$$
$$\zeta = b\varepsilon_v + \frac{1}{M}\delta p, \tag{6}$$

where $\mathbf{C}_{dr}$ is the rank-4 drained elasticity tensor, $\mathbf{1}$ is the rank-2 identity tensor, $\boldsymbol{\varepsilon}$ is the linearized strain tensor, defined as the symmetric gradient of the displacement vector $\boldsymbol{u}$,

$$\boldsymbol{\varepsilon} := \frac{1}{2}\left(\nabla\boldsymbol{u} + \nabla^T\boldsymbol{u}\right), \tag{7}$$

and $\varepsilon_v = \mathrm{tr}\,(\boldsymbol{\varepsilon})$ is the volumetric strain. Note that we use the convention that tensile stress is positive. It is useful to express the strain tensor as the sum of its volumetric and deviatoric components:

$$\boldsymbol{\varepsilon} = \frac{1}{3}\varepsilon_v\mathbf{1} + \boldsymbol{e}, \tag{8}$$

from which it follows that the volumetric stress $\sigma_v = \mathrm{tr}\,(\boldsymbol{\sigma})/3$ satisfies

$$\delta\sigma_v = K_{dr}\varepsilon_v - b\delta p. \tag{9}$$

Equation (6) implies that the effective stress in single-phase poroelasticity, responsible for skeleton deformation, is defined in incremental form as

$$\delta\boldsymbol{\sigma}' := \delta\boldsymbol{\sigma} + b\delta p\mathbf{1}. \tag{10}$$

Biot's theory of poroelasticity has two coupling coefficients: the Biot modulus M and the Biot coefficient b. They are related to rock and fluid properties as [*Coussy*, 1995]

$$\frac{1}{M} = \phi_0 c_f + \frac{b - \phi_0}{K_s}, \quad b = 1 - \frac{K_{dr}}{K_s}, \tag{11}$$

where $c_f = 1/K_f$ is the fluid compressibility, K_f is the bulk modulus of the fluid, K_s is the bulk modulus of the solid grain, and K_{dr} is the drained bulk modulus of the porous medium.

To set the stage for the numerical solution strategy of the coupled problem, it is useful to write the fluid mass balance equation (3) (the pressure equation) in a way that explicitly recognizes the coupling with mechanical deformation. Equation (6) state that the increment in fluid mass content has two components: increment due to expansion of the pore space and increment due to increase in the fluid pressure. Assuming small elastic deformations and applying linearization from the reference state to the current state, we can write equation (6) as

$$\boldsymbol{\sigma} - \boldsymbol{\sigma}_0 = \mathbf{C}_{dr} : \boldsymbol{\varepsilon} - b(p - p_0)\mathbf{1}, \tag{12}$$

$$\frac{1}{\rho_{f,0}}(m - m_0) = b\varepsilon_v + \frac{1}{M}(p - p_0). \tag{13}$$

Substituting equation (13) into equation (3), we obtain the fluid mass balance equation in terms of the pressure and the volumetric strain:

$$\frac{1}{M}\frac{\partial p}{\partial t}+b\frac{\partial \varepsilon_v}{\partial t}+\nabla \cdot \mathbf{v}=f. \tag{14}$$

Linearizing the relation between volumetric total stress and volumetric strain with respect to the reference state,

$$\sigma_v-\sigma_{v,0}=K_{dr}\varepsilon_v-b(p-p_0), \tag{15}$$

allows us to express the change in porosity as the sum of a volumetric stress component and a fluid pressure component. From $m=\rho_f \phi$ and equation (13),

$$\frac{\rho_f}{\rho_{f,0}}\phi-\phi_0=\frac{b}{K_{dr}}\left(\sigma_v-\sigma_{v,0}\right)+\left(\frac{b^2}{K_{dr}}+\frac{1}{M}\right)(p-p_0). \tag{16}$$

Using the effective stress equation (15), we can rewrite equation (14) in terms of pressure and volumetric total stress:

$$\left(\frac{b^2}{K_{dr}}+\frac{1}{M}\right)\frac{\partial p}{\partial t}+\frac{b}{K_{dr}}\frac{\partial \sigma_v}{\partial t}+\nabla \cdot \mathbf{v}=f. \tag{17}$$

Note that equations (14) and (17) are exactly equivalent. They both recognize the two-way poromechanical coupling, but they lead naturally to different operator splits in a sequential solution method: the fixed-strain split and the fixed-stress split, respectively [*Kim et al.*, 2011b, 2011c]. Note that, by virtue of the poromechanical coupling, quantities like fluid compressibility and rock compressibility do not appear explicitly in the equation. Instead, the fluid-rock compressibility behavior is determined from the poroelastic coefficients K_{dr}, b, and M [*Kim et al.*, 2011b].

2.3. Multiphase Poromechanics

In the multiphase or partially saturated fluid system, it is not possible to linearize equation (6) around a reference state because [*Coussy*, 1995]:

1. Gases are very compressible.

2. Capillary pressure effects are intrinsically nonlinear.

3. Phase saturations vary between 0 and 1 and, therefore, a typical problem samples the entire range of nonlinearity.

Therefore, following *Coussy* [1995], we use the incremental formulation of poromechanics for multiphase systems, which does not assume physical linearization of total stress from the initial state to the current (deformed) state.

To make progress, we make a modeling assumption that allows us to express the deformation of a multiphase porous material in terms of the increment in applied total stresses and internal fluid pressures. Similar to the single-phase case (equation (6)), we adopt an effective stress formulation in the multiphase poromechanics [*Bishop*, 1959; *Bishop and Blight*, 1963] because constitutive modeling of porous materials is usually done in terms of the effective stress. Under this formulation, we split the total stress on the porous material into two parts: one that is responsible for deformation of the solid skeleton (the effective stress), and another component that is responsible for changes in the fluid pressures

$$\delta\boldsymbol{\sigma}=\mathbf{C}_{dr}:\delta\boldsymbol{\varepsilon}-\sum_{\beta}b_{\beta}\delta p_{\beta}\mathbf{1}, \tag{18}$$

where b_{β} are the Biot coefficients for individual phases such that $\sum_{\beta}b_{\beta}=b$, where b is the Biot coefficient of the saturated porous material. It is common to further assume that b_{β} are proportional to the respective saturations S_{β} [*Lewis and Sukirman*, 1993; *Coussy et al.*, 1998; *Lewis and Schrefler*, 1998].

The effective stress concept allows us to treat a multiphase porous medium as a mechanically equivalent single-phase continuum [*Khalili et al.*, 2004; *Nuth and Laloui*, 2008]. The appropriate form of the effective stress equation in a multiphase system is still an active area of research [*Gray and Schrefler*, 2001; *Coussy et al.*, 2004; *Nuth and Laloui*, 2008; *Vlahinic et al.*, 2011; *Nikooee et al.*, 2013; *Kim et al.*, 2013]. Here we use the concept of *equivalent pressure* [*Coussy et al.*, 2004] in the effective stress equation (equation (18))

$$p_E = \sum_{\beta} S_{\beta} p_{\beta} - U, \tag{19}$$

where $U = \sum_{\beta} \int p_{\beta} dS_{\beta}$ is the interfacial energy computed from the capillary pressure relations [*Kim et al.*, 2013]. The equivalent pressure accounts for the interface energy in the free energy of the system and leads to a thermodynamically consistent and mathematically well-posed description of the multiphase fluid response to the solid deformation [*Kim et al.*, 2013]. For a system with two phases, the wetting phase w and the nonwetting phase g, the capillary pressure is

$$P_c(S_w) \equiv P_{wg}(S_w) = p_g - p_w, \tag{20}$$

and the interfacial energy is $U = \int_{S_w}^{1} P_{wg} dS$. Assuming $b_{\beta} = bS_{\beta}$ [*Lewis and Sukirman*, 1993; *Coussy et al.*, 1998; *Lewis and Schrefler*, 1998] and using equation (19) in equation (18), we obtain the stress-strain relationship for multiphase linear poroelasticity:

$$\delta\boldsymbol{\sigma} = \delta\boldsymbol{\sigma}' - b\delta p_E \mathbf{1}, \quad \delta\boldsymbol{\sigma}' = \mathbf{C}_{dr} : \delta\boldsymbol{\varepsilon}. \tag{21}$$

Once we have a definition of the effective stress in multiphase systems, we now express the change in the fluid mass in terms of the mechanical deformation and the change in the fluid pressures. In the deformed configuration, the mass of phase α per unit volume of porous medium is

$$m_{\alpha} = \rho_{\alpha} S_{\alpha} \phi (1 + \varepsilon_v). \tag{22}$$

Note that, by definition, the sum of all fluid phase saturations satisfies $\sum_{\beta}^{n_{\text{phase}}} S_{\beta} \equiv 1$. Extending equation (13) for multiphase systems [*Coussy*, 1995, 2004], we have

$$\left(\frac{dm}{\rho}\right)_{\alpha} = b_{\alpha} d\varepsilon_v + \sum_{\beta} N_{\alpha\beta} dp_{\beta}, \tag{23}$$

where $\mathbf{N} = \mathbf{M}^{-1}$ is the inverse Biot modulus. In a multiphase system, the Biot modulus is a symmetric positive definite tensor $\mathbf{M} = [M_{\alpha\beta}]$, and the Biot coefficient is a vector. To determine the coupling coefficients $N_{\alpha\beta}$ as a function of the primary variables (pressure, saturations, and displacement), and rock and fluid properties, we develop an alternate expression for the differential increment in fluid mass. Using equation (22),

$$dm_{\alpha} = d(\rho_{\alpha} S_{\alpha} \phi (1 + \varepsilon_v)), \tag{24}$$

which can be expanded as

$$\left(\frac{dm}{\rho}\right)_{\alpha} = \phi \frac{\partial S_{\alpha}}{\partial P_{\alpha\beta}} dP_{\alpha\beta} + \phi S_{\alpha} c_{\alpha} dp_{\alpha} + \phi S_{\alpha} d\varepsilon_v + S_{\alpha} d\phi, \tag{25}$$

where $c_{\alpha} = \frac{1}{\rho_{\alpha}} \frac{d\rho_{\alpha}}{dp_{\alpha}}$ is the compressibility of the fluid phase α, and $\partial S_{\alpha} / \partial P_{\alpha\beta}$ is the inverse capillary pressure derivative. Above, repeated indices do not imply summation and we have assumed infinitesimal deformations. We can express the increment in porosity, $d\phi$, as a function of the volumetric effective stress, $d\sigma'_v$, to

obtain a closed-form expression of equation (25). Let $V_s = V_b - V_p$ be the volume of the solid matrix, and $d\varepsilon_{sv} = dV_s/V_s = d\sigma_{sv}/K_s$ be the volumetric dilation of the solid matrix, where σ_{sv} is the volumetric matrix stress. From $d\phi = d(V_p/V_b) = \phi(dV_p/V_p - dV_b/V_b)$, we can write the incremental form of strain partition as

$$(1-\phi)d\varepsilon_v = (1-\phi)d\varepsilon_{sv} + d\phi. \qquad (26)$$

Similarly, the volumetric Cauchy total stress can be partitioned into the volumetric matrix stress and the fluid pressure as

$$d\sigma_v = (1-\phi)d\sigma_{sv} - \phi dp_E. \qquad (27)$$

Substituting $d\sigma_{sv}$ from equation (27) into equation (26), we obtain

$$d\phi = \frac{b-\phi}{K_{dr}}\left(d\sigma_v' + (1-b)dp_E\right). \qquad (28)$$

Equation (28) implies that an increment in porosity is related to increments in volumetric effective stress and fluid pressures, similar to equation (16) in the single-phase case. Substituting $d\varepsilon_v$ from equation (21) and $d\phi$ from equation (28) into equation (25) allows us to express the increment in the phase mass as a function of the increments in the total volumetric stress and phase pressures. Equating this to equation (23) yields the desired expressions for the coupling coefficients $N_{\alpha\beta}$, which for a water-gas system are

$$N_{gg} = -\phi\frac{\partial S_w}{\partial P_{wg}} + \phi S_g c_g + S_g^2 N,$$

$$N_{gw} = N_{wg} = \phi\frac{\partial S_w}{\partial P_{wg}} + S_g S_w N, \qquad (29)$$

$$N_{ww} = -\phi\frac{\partial S_w}{\partial P_{wg}} + \phi S_w c_w + S_w^2 N,$$

where $N = (b-\phi)(1-b)/K_{dr}$, and the subscripts w and g denote water and gas phases, respectively.

Finally, we obtain the multiphase flow equation for phase α in a poroelastic medium by substituting the two constitutive relations, the effective stress equation (equation (21)) and the fluid mass increment equation (equation (23)) in the mass balance equation (equation (2)):

$$\frac{\partial}{\partial t}\left(\rho_\alpha \sum_\beta \left(N_{\alpha\beta} + \frac{b_\alpha b_\beta}{K_{dr}}\right)p_\beta\right) + \frac{1}{K_{dr}}\frac{\partial}{\partial t}(\rho_\alpha b_\alpha \sigma_v) + \nabla \cdot \boldsymbol{w}_\alpha = \rho_\alpha f_\alpha, \quad \forall\alpha = 1,\ldots,n_{\text{phase}}. \qquad (30)$$

The role of $\boldsymbol{N}$ and $\boldsymbol{b}$ as the coupling coefficients among different fluid phases and the solid phase is evident from the above equation. The bulk density ρ_b in the mechanical equilibrium equation (equation (1)) also acts as a coupling parameter because it is a function of the porosity and the phase saturations. Because we assume that the fluids are immiscible, the mass flux of phase α is $\boldsymbol{w}_\alpha = \rho_\alpha \boldsymbol{v}_\alpha$, where we adopt the traditional multiphase flow extension of Darcy's law [*Muskat*, 1949; *Bear*, 1972]:

$$\boldsymbol{v}_\alpha = -\frac{\boldsymbol{k} k_\alpha^r}{\mu_\alpha}(\nabla p_\alpha - \rho_\alpha \boldsymbol{g}), \qquad (31)$$

where μ_α and k_α^r are the dynamic viscosity and the relative permeability of phase α in the presence of other fluid phases.

2.4. Poromechanics of Faults
There are two basic approaches to represent faults in a three-dimensional medium: either as a three-dimensional fault zone [e.g., *Rutqvist et al.*, 2008] or a two-dimensional fault surface [e.g., *Juanes et al.*, 2002; *Molinero et al.*,
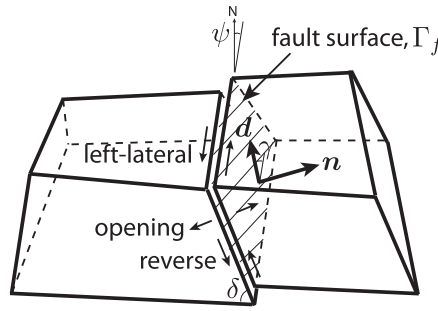
Figure 1. Schematic of a 2-D fault surface in a 3-D domain. Discontinuity in the displacement across the fault is illustrated through the slip vector, **d**, on the fault. Here slip is assumed to be in the fault plane with no opening. The fault normal vector **n**, strike angle ψ, dip angle δ, and slip rake angle γ are defined in the global coordinate system. The fault coordinate system is defined in terms of tangential and normal motion on the fault with positive values associated with left-lateral, reverse, and opening motions.

2002; *Ferronato et al.*, 2008]. The advantage of representing faults as surfaces of discontinuity is that they can more faithfully describe the localized (discontinuous) displacement at the fault, and that one can incorporate models of dynamic frictional strength (like the rate- and state-friction model) capable of reproducing runaway fault slip characteristic of earthquakes. Moreover, introducing discrete fault surfaces does not preclude modeling an adjacent fault zone with appropriate rheology.

A central feature of our work is that we treat faults as surfaces of discontinuity embedded in the continuum, across which displacement is allowed to be discontinuous to recognize the possibility of fault slip (Figure 1). We use zero-thickness elements, also known as interface elements or cohesive elements in the finite element literature [*Goodman et al.*, 1968; *Beer*, 1985; *Carol et al.*, 1985; *Gens et al.*, 1988; *Lei et al.*, 1995], to represent the fault surfaces. Mathematically, the fault surface is treated as an interior boundary between the two adjacent domains. The two sides of the fault surface, which need not be planar, are designated as the "+" side and the "−" side, and the fault normal vector **n** points from the negative side to the positive side. Slip on the fault is the displacement of the positive side relative to the negative side

$$(\boldsymbol{u}_{+}-\boldsymbol{u}_{-})-\boldsymbol{d}=\boldsymbol{0} \text{ on } \Gamma_f, \tag{32}$$

where $\boldsymbol{u}_{+}$ and $\boldsymbol{u}_{-}$ are the displacements on the two sides of the fault surface, denoted by Γ_f, and $\boldsymbol{d}$ is the fault slip vector. Fault slip is governed by the effective traction on the fault, which is a function of the effective stress tensors on both sides of the fault, the fault normal direction, and the fault constitutive law. We impose the *effective* traction on the fault by introducing a Lagrange multiplier, $\boldsymbol{l}$, which is a force per unit area required to satisfy the equilibrium equation for a given relative displacement, $\boldsymbol{d}$, across the fault. The magnitude of the effective normal traction on the fault is

$$\sigma'_n=\boldsymbol{l} \cdot \boldsymbol{n}. \tag{33}$$

A positive value of σ'_n indicates that a tensile effective stress is transmitted across the fault surface. The Kuhn-Tucker conditions of contact mechanics are obeyed such that no penetration occurs and the effective normal traction stays compressive at the contact surface. The shear traction vector is, by definition, tangent to the fault surface and its magnitude is

$$\tau=|\boldsymbol{l}-\sigma'_n\boldsymbol{n}|. \tag{34}$$

2.4.1. Models of Fault Strength

Shear tractions on the fault are limited by fault friction, or fault strength. A fault constitutive model is used to compute the frictional stress τ_f on the fault as

$$\tau_f=\begin{cases} \tau_c-\mu_f\sigma'_n, & \sigma'_n < 0, \\ \tau_c, & \sigma'_n \geq 0, \end{cases} \tag{35}$$

where τ_c is the cohesive strength of the fault and μ_f is the coefficient of friction. Note, again, that we use

the convention that tensile stress is positive. The coefficient of friction μ_f is modeled as a function of displacement evolution on the fault. Commonly used fault friction models are:

1. Static friction model, where μ_f is a constant.

2. Slip-weakening model, where μ_f is a function of the slip magnitude $|\boldsymbol{d}|$, and drops linearly from its static value, μ_s, to its dynamic value, μ_d, over a critical slip distance d_c

$$
\mu_f = \begin{cases} \mu_s - (\mu_s - \mu_d)\dfrac{|\boldsymbol{d}|}{d_c}, & |\boldsymbol{d}| \leq d_c, \\ \mu_d, & |\boldsymbol{d}| > d_c. \end{cases} \tag{36}
$$

3. Rate- and state-dependent friction model [*Dieterich*, 1979, 1981; *Ruina*, 1983; *Scholz*, 1989; *Marone*, 1998],

$$
\begin{aligned}
\mu_f &= \mu_0 + A \ln\left(\frac{V}{V_0}\right) + B \ln\left(\frac{V_0 \theta}{d_c}\right), \\
\frac{d\theta}{dt} &= 1 - \frac{\theta V}{d_c},
\end{aligned} \tag{37}
$$

where $V = |d\boldsymbol{d}/dt|$ is the slip rate magnitude, μ_0 is the steady state friction coefficient at the reference slip rate V_0, A and B are empirical dimensionless constants, and θ is the macroscopic variable characterizing state of the surface.

In the rate- and state-dependent friction model, which is based on laboratory experiments of frictional sliding on rock surfaces and fault gouges, the evolution of the coefficient of friction is determined from the combined effect of the evolution of the state variable, θ, and the slip rate or velocity, V. Here θ may be understood as the frictional contact time [*Dieterich*, 1979], or the average maturity of contact asperities between the sliding surfaces [*Rice*, 1993]. The evolution of θ is assumed to be independent of changes in the normal traction, σ'_n, that can accompany the fault slip due to changes in fluid pressure. The model accounts for the decrease in friction (slip-weakening) as the slip increases, and the increase in friction (healing) as the time of contact or slip velocity increases (Figure 2). The two effects act together such that $A > B$ leads to strengthening of the fault, stable sliding, and creeping motion, and $A < B$ leads to weakening of the fault, frictional instability, and accelerating slip. In this way, the model is capable of capturing repetitive stick-slip behavior of faults and the resulting seismic cycle [*Dieterich*, 1981; *Scholz*, 1989].

We use the Mohr-Coulomb theory to define the stability criterion for the fault [*Jaeger and Cook*, 1979]. When the shear traction on the fault is below the friction stress, $\tau \leq \tau_f$, the fault does not slip. When the shear traction is larger than the friction stress, $\tau > \tau_f$, the contact problem is solved to determine the Lagrange multipliers and slip on the fault, such that the Lagrange multipliers are compatible with the frictional stress.

2.4.2. Fault Pressure in the Failure Criterion

Traditionally, in the Andersonian faulting theory [*Anderson*, 1951], fault slip is modeled in a "dry environment," that is, in the absence of fluids. While, in some cases, the presence of fluid has been recognized through the effective stress concept, the dynamics of flow was not included for reasons of conceptual and computational simplicity, as well as for the belief that fluid flow played a secondary role in the release of tectonic stresses [*Hubbert and Rubey*, 1959; *Reasenberg and Simpson*, 1992]. The effect of pore pressure was accounted for by modifying the coefficient of fault friction μ_f [*Harris and Simpson*, 1992; *Harris et al.*, 1995], an approach later suggested to be "unwise" [*Beeler et al.*, 2000]. In the case of mature faults, the fault core permeability can be low due to comminution of grains while the damaged host rock permeability can be high due to fractures [*Sibson*, 1977, 1986; *Chester et al.*, 1993; *Caine and Forster*, 1999]. In addition, the permeability can vary substantially across the fault during the seismic cycle [*Sibson*, 1981, 1990]. As a result, pore pressures can be significantly different across the fault [*Sibson*, 1994; *Rice*, 1992; *Chester et al.*, 1993].

A difference in fluid pressure across the fault leads to a pressure jump $[\![p]\!]_{\Gamma_f} = p_+ - p_-$, where p_+ and p_- are the equivalent multiphase pressures (equation (19)) on the "positive" and the "negative" side of the fault. One of the key features of the 2-D representation of faults is the ability to reproduce a finite jump in the

pressure, $[\![p]\!]_{\Gamma_f}$, across the fault. This pressure jump leads to a discontinuity in the effective stress across the fault, such that the total stress is continuous

$$\boldsymbol{\sigma}'_- \cdot \boldsymbol{n} - bp_- \boldsymbol{n} = \boldsymbol{\sigma}'_+ \cdot \boldsymbol{n} - bp_+ \boldsymbol{n}, \tag{38}$$

a requirement for momentum balance on the fault. This gives rise to the question of how to incorporate in the formulation the pressure jump across a fault. This is important because it determines the stability of the fault.

Fault stability can be assessed by evaluating the stability criterion on both sides of the fault separately. The side of the fault where the criterion is met first determines the fault stability. Equivalently, this can be achieved by defining a *fault pressure* that is a function of the pressures on the two sides, p_+ and p_-. Introducing the fault pressure allows us to uniquely define the *effective* normal traction on the fault, σ'_n, and determine the fault friction τ_f (equation (35)). Since the stability criterion, $\tau < \tau_f$, is first violated with the larger pressure, we define the fault pressure, p_f, as

$$p_f = \max(p_-, p_+). \tag{39}$$

Our definition of fault pressure is a natural result of our fault representation, rather than a conservative assumption. Note that estimating the fault pressure as the arithmetic average of the pressures on the two sides, as proposed in the case of tensile fractures [*Segura and Carol*, 2004, 2008a, 2008b], may incorrectly delay the onset of shear failure. By univocally defining the pressure at the fault (equation (39)), we also univocally define the effective traction at the fault (the Lagrange multiplier *l*), something that is required to evaluate the fault stability criterion.

2.5. Boundary and Initial Conditions

The mathematical model requires that initial and boundary conditions be defined for both the fluid flow and mechanical problems. We consider one pressure, p_α, and $n_{phase} - 1$ saturations, $\{S_\beta, \forall \beta \neq \alpha\}$, as the primary variables of the multiphase flow problem, where α is one of the fluid phases. Pressures of the remaining $n_{phase} - 1$ phases can be uniquely determined from the $n_{phase} - 1$ capillary pressure relations (equation (20)). Saturation S_α is determined from the constraint that the sum of all saturations is identically equal to 1.

Geologic reservoirs are located at depth, while the effect of coupled flow and deformation, such as subsidence and earthquakes, is observed at the ground surface. The weight of the overburden rock plays an important role in determining the ground subsidence even when it is not part of the flow domain. The flow domain could also be laterally confined due to sedimentary or stratigraphic features such as pinch-outs, sealing faults, or other types of hydraulic barriers. As a result, the boundaries of the flow domain and the mechanical domain may not coincide. The mechanical domain is usually extended such that it encapsulates the flow domain [*Settari and Mourits*, 1998]. This extended mechanics domain is needed for reducing spurious boundary effects, especially because the stress conditions at depth are rarely known with certainty.

Since the flow equation (equation (30)) is a statement of balance of fluid fluxes with fluid accumulation, the most natural boundary condition for the flow problem is a flux boundary condition. It is a common practice to define the flow domain such that it can be modeled as a closed system, in which case the normal component of the fluid flux of each phase α across the boundary is zero

$$\boldsymbol{v}_\alpha \cdot \boldsymbol{n} = 0 \text{ on } \Gamma_v, \tag{40}$$

where $\boldsymbol{n}$ is the outward unit normal to the boundary Γ_v. Nonzero boundary fluxes can similarly be prescribed. When the flow domain is in communication with an external system with known pressure (such as an aquifer of known capacity), it is possible to prescribe a mixed boundary condition, where a linear combination of pressure and normal pressure gradient across the boundary, for a given phase, is expressed in terms of the pressure outside the boundary
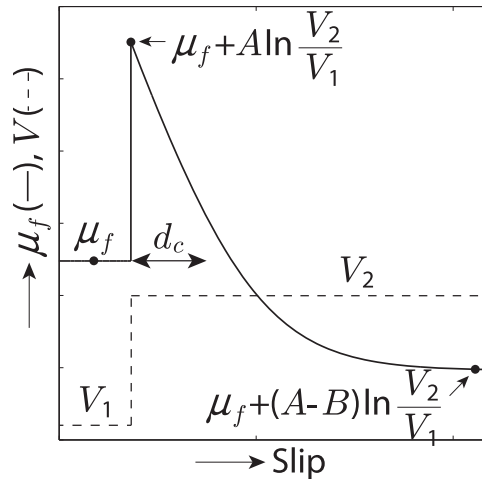
Figure 2. Rate- and state-dependent friction model. The coefficient of friction on the fault, μ_f, evolves with the slip rate or velocity, V, and the state variable, θ (equation (37)). For a sudden increase in the slip velocity from V_1 to V_2, the coefficient of friction first increases sharply due to a sudden increase in resistance from contact asperities and then declines slowly due to slip-weakening. The final steady state value of the coefficient of friction can be lower than the initial steady state value if $A - B < 0$, as shown above.

$$C_1 \frac{\partial p_\alpha}{\partial n} + p_\alpha = \bar{p} \text{ on } \Gamma_p, \quad (41)$$

where C_1 is a constant related to the boundary transmissibility and $\bar{p}$ is the known external pressure [*Carter and Tracy*, 1960; *Fetkovich*, 1971]. The parts of the boundary with prescribed external pressure and flux must be nonoverlapping and cover the entire boundary, i.e., $\Gamma_p \cap \Gamma_v = \emptyset$, $\Gamma_p \cup \Gamma_v = \partial\Omega$.

For the mechanical problem, displacements are the primary variables. The boundary condition can be prescribed either in terms of the displacements or the tractions or a suitable combination of both along the boundary

$$\boldsymbol{u} = \bar{\boldsymbol{u}} \text{ on } \Gamma_u, \quad \boldsymbol{\sigma} \cdot \boldsymbol{n} = \bar{\boldsymbol{t}} \text{ on } \Gamma_\sigma, \quad (42)$$

where $\bar{\boldsymbol{u}}$ is a prescribed displacement and $\bar{\boldsymbol{t}}$ is a prescribed traction. Γ_u and Γ_σ boundaries may overlap because a node can have a prescribed displacement in one direction and prescribed tractions in other directions. However, they must satisfy $\Gamma_u \cup \Gamma_\sigma = \partial\Omega$.

Initialization of a coupled multiphase poromechanics problem is not trivial. The common practice is to initialize the problem under the assumption of flow and mechanical equilibrium. Pressures and saturations in the multiphase flow problem can be initialized using the concept of Vertical Equilibrium [*Dake*, 1978], which assumes that the fluids are distributed vertically satisfying capillary-gravity equilibrium. Since initialization is performed at a time before any well starts to flow, this is usually a good assumption. Initial pressures are calculated based on hydrostatics, using prescribed fluid contacts and a datum pressure in the flow domain. Initial saturations are calculated from the initial capillary pressures, and they also honor the fluid contacts. Since hydrostatic pressures depend on fluid densities, which in turn depend on fluid compressibilities, which further depend on pressures, initialization is done iteratively; two to three iterations are sufficient for most problems.

We initialize the mechanical problem with a zero-displacement field. Therefore, initial stresses are prescribed such that they balance body forces and boundary tractions.

3. Numerical Formulation

In this section, we discuss the numerical formulation and discretization of the coupled multiphase flow and geomechanics problem. We first present the space discretization, followed by the time discretization and, finally, the fully discrete system of algebraic equations.

3.1. Space Discretization

We use the finite volume method for the discretization of the flow problem [*Aziz and Settari*, 1979] and the nodal-based finite element method for the discretization of the mechanics problem [*Hughes*, 1987; *Zienkiewicz and Taylor*, 2005]. We use a single, unstructured computational grid for both flow and mechanics problems. The pressures and saturations degrees of freedom are located at the element center, and the displacement vector degrees of freedom are located at the element nodes (Figure 3). This space discretization is locally mass conservative at the element level and enjoys excellent stability properties [*Jha and Juanes*, 2007; *Phillips and Wheeler*, 2007a, 2007b; *Kim et al.*, 2011c].
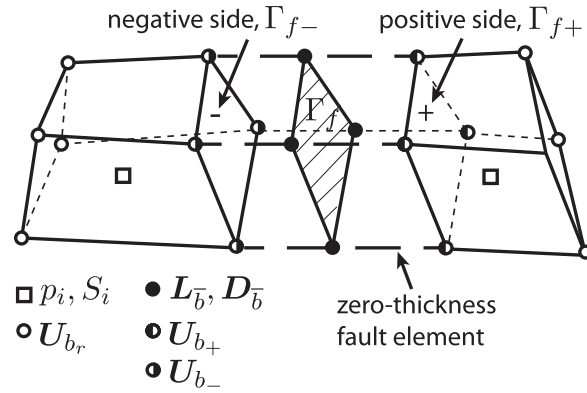
Figure 3. Exploded view of our computational representation of a fault, illustrating different node types, locations of different variables, and the zero-thickness fault element. Fluid pressures p_i and saturations S_i are located at the element centers as they are discretized using the finite volume method. Displacements and Lagrange multipliers at the fault are discretized using the nodal-based finite element method. There are two types of nodes in the domain: the displacement nodes and the Lagrange nodes. The displacement nodes carry the displacements U_{b_r} at the regular nodes, the displacements U_{b_+} on the positive side of the fault, and the displacements U_{b_-} on the negative side of the fault. The Lagrange nodes carry two types of fault variables: the Lagrange multipliers $L_{\bar{b}}$ (related to fault tractions) and the fault slip $D_{\bar{b}}$. The displacement nodes on the positive and negative sides and the Lagrange nodes are collocated in the initial grid.

Elements with nodes on the fault surface deserve special consideration. Each node on the fault is triplicated to create a "+" node on the positive side, a "−" node on the negative side, and a Lagrange node in the middle. The side nodes store the positive side displacement u_+ and the negative side displacement u_-, respectively. The Lagrange node stores the Lagrange multiplier l and the fault slip d. All three nodes are physically collocated in the initial grid, so elements representing the fault are *zero-thickness elements*. Slip on the fault is related to the positive and the negative side displacement fields through equation (32). The Lagrange multipliers are the effective fault tractions required to satisfy both the equilibrium equation (equation (43)), and the stability criterion

$\tau \leq \tau_f$ with τ_f from equation (35). We define a fault coordinate system to relate the quantities commonly used in describing the fault motion (reverse or normal slip, and left-lateral or right-lateral slip; see Figure 1) to the global displacements. In three dimensions, the fault coordinate system is defined with along-strike (lateral), along-dip (reverse or normal), and normal-to-fault (opening) directions (Figure 1). In the fault coordinate system, the fault normal vector in 3-D is $n_f = [0, 0, 1]^T$, where superscript T indicates transpose.

3.1.1. Mechanics Problem

Using standard arguments from functional analysis [*Brezis*, 2011], that is, multiplying by the test functions (which act as weighting functions in the integral form of the differential equation, and satisfy essential boundary conditions), integrating over the domain, applying the divergence theorem, inserting the essential and natural boundary conditions, and exploiting symmetry of the stress tensor, we arrive at the weak form of the governing equations for the mechanics problem: Find (u, l) belonging to appropriate functional spaces satisfying the essential boundary conditions ($u = \bar{u}$ on Γ_u) such that

$$\int_\Omega \nabla^s \eta : (\sigma' - bp_E \mathbf{1})d\Omega + \int_{\Gamma_{f_+}} \eta \cdot (l - bp_f n)d\Gamma - \int_{\Gamma_{f_-}} \eta \cdot (l - bp_f n)d\Gamma - \int_\Omega \eta \cdot \rho_b g d\Omega - \int_{\Gamma_\sigma} \eta \cdot \bar{t} d\Gamma = 0, \tag{43}$$

$$\int_{\Gamma_{f_+}} \eta \cdot u_+ d\Gamma - \int_{\Gamma_{f_-}} \eta \cdot u_- d\Gamma - \int_{\Gamma_f} \eta \cdot d d\Gamma = 0, \tag{44}$$

for all test functions η ($n_{\text{dim}} \times 1$ vector) belonging to the appropriate functional space satisfying $\eta = 0$ on Γ_u. Here we used the multiphase effective stress equation (equation (21)), p_E is the equivalent pressure (equation (19)), p_f is the fault pressure (equation (39)), and ρ_b is the bulk density, all of which depend on the phase pressures and saturations, and, therefore, on the solution of the flow problem.

Let the domain be partitioned into nonoverlapping elements (grid blocks), $\Omega = \overset{n_{\text{elem}}}{\underset{j=1}{\cup}} \Omega_j$, where n_{elem} is the number of volumetric elements. A fault is treated as an interior boundary with its domain, Γ_f, partitioned into nonoverlapping fault elements, $\Gamma_f = \overset{n_{f,\text{elem}}}{\underset{j=1}{\cup}} \Gamma_{f,j}$, where the subscript f indicates variables associated with a fault. The displacement, the Lagrange multiplier, and the slip fields are approximated as follows:

$$u \approx u_h = \sum_{b=1}^{n_{node}} \eta_b U_b, \tag{45}$$

$$l \approx l_h = \sum_{\bar{b}=1}^{n_{f,node}} \eta_{\bar{b}} L_{\bar{b}}, \tag{46}$$

$$d \approx d_h = \sum_{\bar{b}=1}^{n_{f,node}} \eta_{\bar{b}} D_{\bar{b}}, \tag{47}$$

where subscript h indicates the finite element approximation, n_{node} is the number of displacement nodes (including the duplicated nodes at the fault elements; see Figure 3), and $n_{f,node}$ is the number of Lagrange nodes. U_b is the $n_{dim} \times 1$ vector of nodal displacements for node b in the domain coordinate system, $U_b = (U_{b,x}, U_{b,y}, U_{b,z})$. $L_{\bar{b}}$ and $D_{\bar{b}}$ are the $n_{dim} \times 1$ Lagrange multiplier and slip vectors at Lagrange node $\bar{b}$ of the fault, and they are in the fault coordinate system (left-lateral, reverse, and opening, respectively; see Figure 1): $L_{\bar{b}} = (L_{\bar{b},1}, L_{\bar{b},2}, L_{\bar{b},3})$ and $D_{\bar{b}} = (D_{\bar{b},1}, D_{\bar{b},2}, D_{\bar{b},3})$.

The interpolation functions, η_b and $\eta_{\bar{b}}$, are the usual C^0-continuous isoparametric functions, such that they take a value of 1 at the respective nodes, and 0 at all other nodes [*Hughes*, 1987]. In a Galerkin method, the test functions are chosen to be equal to the interpolation functions.

After substitution of the finite element approximations into the weak form of the problem (equations (43) and (44)), we obtain the discrete equations in residual form at all displacement nodes a and all Lagrange nodes $\bar{a}$:

$$0 = \int_\Omega B_a^T (\sigma'_h - b p_{E,h} \mathbf{1}) d\Omega \quad + \int_{\Gamma_{f_+}} \eta_a^T (l_h - b p_{f,h} n) d\Gamma - \int_{\Gamma_{f_-}} \eta_a^T (l_h - b p_{f,h} n) d\Gamma$$

$$- \int_\Omega \eta_a^T \rho_{b,h} g \, d\Omega - \int_{\Gamma_\sigma} \eta_a^T \bar{t} \, d\Gamma \quad \forall a = 1, \ldots, n_{node}, \tag{48}$$

$$0 = \int_{\Gamma_{f_+}} \eta_{\bar{a}}^T u_{h_+} d\Gamma - \int_{\Gamma_{f_-}} \eta_{\bar{a}}^T u_{h_-} d\Gamma - \int_{\Gamma_f} \eta_{\bar{a}}^T d_h d\Gamma \quad \forall \bar{a} = 1, \ldots, n_{f,node}, \tag{49}$$

where we have defined the nodal matrices for the shape function

$$\eta_a = \begin{bmatrix} \eta_a & 0 & 0 \\ 0 & \eta_a & 0 \\ 0 & 0 & \eta_a \end{bmatrix} \tag{50}$$

and its symmetric gradient

$$B_a = \begin{bmatrix} \partial_x \eta_a & 0 & 0 \\ 0 & \partial_y \eta_a & 0 \\ 0 & 0 & \partial_z \eta_a \\ \partial_y \eta_a & \partial_x \eta_a & 0 \\ 0 & \partial_z \eta_a & \partial_y \eta_a \\ \partial_z \eta_a & 0 & \partial_x \eta_a \end{bmatrix}, \tag{51}$$

corresponding to the compact engineering notation for stress and strain inside an element, $\sigma'_h = [\sigma'_{h,xx}, \sigma'_{h,yy}, \sigma'_{h,zz}, \sigma'_{h,xy}, \sigma'_{h,yz}, \sigma'_{h,xz}]^T$ and $\varepsilon_h = [\varepsilon_{h,xx}, \varepsilon_{h,yy}, \varepsilon_{h,zz}, 2\varepsilon_{h,xy}, 2\varepsilon_{h,yz}, 2\varepsilon_{h,xz}]^T$, respectively [*Hughes*, 1987]. The identity tensor in compact notation is $\mathbf{1} = [1, 1, 1, 0, 0, 0]^T$.

Equation (48) results in $n_{dim} n_{node}$ equations, and equation (49) results in $n_{dim} n_{f,node}$ equations. We solve equations (48) and (49) subject to the stability criterion, which yields the slip constraint at each Lagrange node $\bar{a}$:

$$\delta \boldsymbol{D}_{\bar{a}} = \begin{cases} \boldsymbol{0}, & \tau_{\bar{a}} \leq \tau_{f,\bar{a}}, \\ \boldsymbol{f}(\boldsymbol{u}_h, \boldsymbol{l}_h, \tau_{f,\bar{a}}), & \tau_{\bar{a}} > \tau_{f,\bar{a}}, \end{cases} \quad \forall \bar{a} = 1, \ldots, n_{f,\text{node}}, \tag{52}$$

where $\delta \boldsymbol{D}_{\bar{a}}$ is the slip increment and τ and τ_f are from equations (34) and (35), respectively. In 3-D, the magnitude of the shear stress is computed from the left-lateral and reverse components of the effective stress at the fault, $\tau_{\bar{a}} = (L_{\bar{a},1}^2 + L_{\bar{a},2}^2)^{1/2}$. $\boldsymbol{f}(\cdot)$ is a vector function of displacements, fault tractions, and fault friction that determines the slip on the fault, and it is determined implicitly during the solution of the contact problem (section 4.1).

3.1.2. Multiphase Flow Problem

The flow problem is discretized using the finite volume method on the same grid defined for the mechanical domain, $\Omega = \bigcup_{i=1}^{n_{\text{elem}}} \Omega_i$. For simplicity, let us consider two fluid phases, water and gas. Note that in each element, $S_w + S_g \equiv 1$. We integrate the fluid phase mass conservation equation (30), for each phase over each element i. For the water phase, this yields

$$\frac{\partial}{\partial t} \int_{\Omega_i} \rho_w \left(\left(N_{ww} + N_{wg} + \frac{bb_w}{K_{dr}} \right) p_g - \left(N_{ww} + \frac{b_w^2}{K_{dr}} \right) P_{wg} \right) d\Omega$$
$$+ \frac{1}{K_{dr}} \frac{\partial}{\partial t} \int_{\Omega_i} \rho_w b_w \sigma_v d\Omega - \int_{\partial \Omega_i} \boldsymbol{w}_w \cdot \boldsymbol{n}_i d\Gamma = \int_{\Omega_i} \rho_w f_w d\Omega, \tag{53}$$

where we used the capillary pressure relation, $P_{wg} = p_g - p_w$, to eliminate the water phase pressure, the Biot coefficient relation, $b_g + b_w = b$, and integration by parts for the mass flux term to express it as a surface integral. $\boldsymbol{n}_i$ is the outward normal to the boundary of element i. Similarly, we have a mass balance equation for the gas phase:

$$\frac{\partial}{\partial t} \int_{\Omega_i} \rho_g \left(\left(N_{wg} + N_{gg} + \frac{bb_g}{K_{dr}} \right) p_g - \left(N_{wg} + \frac{b_g b_w}{K_{dr}} \right) P_{wg} \right) d\Omega$$
$$+ \frac{1}{K_{dr}} \frac{\partial}{\partial t} \int_{\Omega_i} \rho_g b_g \sigma_v d\Omega - \int_{\partial \Omega_i} \boldsymbol{w}_g \cdot \boldsymbol{n}_i d\Gamma = \int_{\Omega_i} \rho_g f_g d\Omega. \tag{54}$$

We approximate both the pressure and the saturation fields with a piecewise constant interpolation function, φ, such that φ_i takes a constant value of 1 over element i and 0 at all other elements. Phase pressures and saturations are approximated as

$$p_\alpha \approx p_{\alpha,h} = \sum_{i=1}^{n_{\text{elem}}} \varphi_i p_{\alpha,i}, \tag{55}$$

$$S_\alpha \approx S_{\alpha,h} = \sum_{i=1}^{n_{\text{elem}}} \varphi_i S_{\alpha,i}, \tag{56}$$

where the discrete pressures, $p_{\alpha,i}$, and phase saturations, $S_{\alpha,i}$, are located at the center of element i (Figure 2).

We can further express the mass flux term as a sum of integral fluxes between element i and its adjacent elements j:

$$\int_{\partial \Omega_i} \boldsymbol{w}_w \cdot \boldsymbol{n}_i d\Gamma = \sum_{j=1}^{n_{\text{face},i}} \int_{\Gamma_{ij}} \boldsymbol{w}_w \cdot \boldsymbol{n}_{ij} d\Gamma = \sum_{j=1}^{n_{\text{face},i}} W_{w,ij}, \tag{57}$$

where $n_{\text{face},i}$ is the number of faces of element i, and $\boldsymbol{n}_{ij}$ is the outward normal at the face Γ_{ij}. The interelement flux of water, $W_{w,ij}$, can be evaluated from Darcy's law (equation (31)) as a function of the rock and fluid properties, pressures, and saturations of element i and its adjacent elements j, using either a two-point or a multipoint flux approximation [*LeVeque*, 2002; *Gunasekera et al.*, 1998; *Aavatsmark*, 2002]. The two-

point flux approximation method uses the flow potentials, $\Phi_{w,i} = p_{w,i} - \rho_{w,i}gz_i$ and $\Phi_{w,j} = p_{w,j} - \rho_{w,j}gz_j$, to approximate the flux through interface ij between two neighboring elements as follows:

$$W_{w,ij} = T_{ij}\lambda_{w,ij}\left(\Phi_{w,i} - \Phi_{w,j}\right),\tag{58}$$

where z_i and z_j are the centroid depths of the elements (with z axis pointing downward), $\lambda_{w,ij}$ is the water phase mobility, and T_{ij} is the geometric transmissibility of the interface Γ_{ij}. The phase mobility is calculated from upstream cells

$$\lambda_{w,ij} = \begin{cases} \rho_{w,i}k^r_{w,i}/\mu_{w,i}, & \text{if } \Phi_{w,i} > \Phi_{w,j}, \\ \rho_{w,j}k^r_{w,j}/\mu_{w,j}, & \text{otherwise}. \end{cases}\tag{59}$$

The geometric transmissibility is estimated from the harmonic average of the respective element permeabilities and element sizes, $T_{ij} = A_{ij}/(\ell_i/k_i + \ell_j/k_j)$, where A_{ij} is the area of the interface, ℓ_i and ℓ_j are the distances between the centroid of the interface and the centroid of the respective adjacent elements, and k_i and k_j are the element permeabilities, assumed isotropic.

After substitution, the semidiscrete water phase mass balance equation is

$$0 = \frac{\partial}{\partial t}\left[V_{b,i}\rho_{w,i}\left(\left(N_{ww} + N_{wg} + \frac{bb_w}{K_{dr}}\right)_i p_{g,i} - \left(N_{ww} + \frac{b_w^2}{K_{dr}}\right)_i P_{wg,i}\right)\right]$$
$$+ \frac{\partial}{\partial t}\left(\rho_{w,i}\left(\frac{b_w\sigma_v}{K_{dr}}\right)_i V_{b,i}\right) - \sum_{j=1}^{n_{\text{face},i}}W_{w,ij} - \rho_{w,i}f_{w,i}V_{b,i}, \quad \forall i = 1, \ldots, n_{\text{elem}},\tag{60}$$

where subscript i refers to the value at element i. Similarly, we could write the semidiscrete equation for the gas phase:

$$0 = \frac{\partial}{\partial t}\left[V_{b,i}\rho_{g,i}\left(\left(N_{gw} + N_{gg} + \frac{bb_g}{K_{dr}}\right)_i p_{g,i} - \left(N_{gw} + \frac{b_g b_w}{K_{dr}}\right)_i P_{wg,i}\right)\right]$$
$$+ \frac{\partial}{\partial t}\left(\rho_{g,i}\left(\frac{b_g\sigma_v}{K_{dr}}\right)_i V_{b,i}\right) - \sum_{j=1}^{n_{\text{face},i}}W_{g,ij} - \rho_{g,i}f_{g,i}V_{b,i}, \quad \forall i = 1, \ldots, n_{\text{elem}}.\tag{61}$$

3.2. Time Discretization
In quasi-static poromechanics, the time derivative appears only in the accumulation term of the fluid mass balance equation (first two terms in equations (60) and (61)) which we approximate using a simple finite difference scheme:

$$\frac{\partial m_\alpha}{\partial t} \approx \delta_t m_\alpha = \frac{m_\alpha^{n+1} - m_\alpha^n}{\delta t},\tag{62}$$

where superscript n denotes the time level, and δt is the time step. We adopt a fully implicit Backward Euler time integration scheme, that is, we evaluate the flux and source/sink terms in equations (60) and (61) at time level $n+1$.

3.3. Fully Discrete Coupled System
Introducing the time discretization in the semidiscrete finite element equations (equations (48) and (49)), we arrive at the following coupled system of algebraic equations:

$$R_{u,a}^{n+1} = \int_\Omega \boldsymbol{B}_a^T (\boldsymbol{\sigma}_h'^{n+1} - bp_{E,h}^{n+1}\boldsymbol{1})d\Omega \quad + \int_{\Gamma_{f_+}} \boldsymbol{\eta}_a^T (\boldsymbol{l}_h^{n+1} - bp_{f,h}^{n+1}\boldsymbol{n})d\Gamma - \int_{\Gamma_{f_-}} \boldsymbol{\eta}_a^T (\boldsymbol{l}_h^{n+1} - bp_{f,h}^{n+1}\boldsymbol{n})d\Gamma$$

$$-\int_\Omega \boldsymbol{\eta}_a^T \rho_{b,h}^{n+1}\boldsymbol{g}d\Omega - \int_{\Gamma_\sigma} \boldsymbol{\eta}_a^T \bar{\boldsymbol{t}}d\Gamma = \boldsymbol{0} \quad \forall a=1,\ldots,n_{\text{node}}, \tag{63}$$

$$R_{l,\bar{a}}^{n+1} = \int_{\Gamma_{f_+}} \boldsymbol{\eta}_{\bar{a}}^T \boldsymbol{u}_{h_+}^{n+1}d\Gamma - \int_{\Gamma_{f_-}} \boldsymbol{\eta}_{\bar{a}}^T \boldsymbol{u}_{h_-}^{n+1}d\Gamma - \int_{\Gamma_f} \boldsymbol{\eta}_{\bar{a}}^T \boldsymbol{d}_h^{n+1}d\Gamma = \boldsymbol{0} \quad \forall \bar{a}=1,\ldots,n_{f,\text{node}}. \tag{64}$$

The global residual vectors are obtained by assembly of the nodal residual vectors:
$\boldsymbol{R}_u = [\boldsymbol{R}_{u,1},\ldots,\boldsymbol{R}_{u,n_{\text{node}}}]^T$, $\boldsymbol{R}_l = [\boldsymbol{R}_{l,1},\ldots,\boldsymbol{R}_{l,n_{f,\text{node}}}]^T$. In vector form, the system of $(n_{\text{dim}} n_{\text{node}} + n_{\text{dim}} n_{f,\text{node}})$ algebraic equations of the mechanical problem reads

$$\begin{bmatrix} \boldsymbol{R}_u \\ \boldsymbol{R}_l \end{bmatrix}^{n+1} = \begin{bmatrix} \boldsymbol{0} \\ \boldsymbol{0} \end{bmatrix}, \tag{65}$$

which needs to be solved for the displacements $\boldsymbol{U}^{n+1} = [\boldsymbol{U}_1^{n+1},\ldots,\boldsymbol{U}_{n_{\text{node}}}^{n+1}]^T$ at the displacement nodes, and the Lagrange multipliers $\boldsymbol{L}^{n+1} = [\boldsymbol{L}_1^{n+1},\ldots,\boldsymbol{L}_{n_{f,\text{node}}}^{n+1}]^T$ at the Lagrange nodes, subject to the constraint $\delta\boldsymbol{D}^{n+1} = [\delta\boldsymbol{D}_1^{n+1},\ldots,\delta\boldsymbol{D}_{n_{f,\text{node}}}^{n+1}]^T = \boldsymbol{0}$ (equation (52)) at every time step.

For the water-gas multiphase flow problem, we have

$$R_{g,i}^{n+1} = \delta_t\left[V_b\rho_g\left(\left(N_{gw}+N_{gg}+\frac{bb_g}{K_{dr}}\right)p_g - \left(N_{gw}+\frac{b_gb_w}{K_{dr}}\right)P_{wg}\right)\right]_i$$

$$+\delta_t\left[\rho_g\frac{b_g}{K_{dr}}\sigma_v V_b\right]_i - \sum_{j=1}^{n_{\text{face},i}} W_{g,ij}^{n+1} - \left[\rho_g^{n+1}f_g^{n+1}V_b\right]_i \quad i=1,\ldots,n_{\text{elem}}, \tag{66}$$

$$R_{w,i}^{n+1} = \delta_t\left[V_b\rho_w\left(\left(N_{ww}+N_{wg}+\frac{bb_w}{K_{dr}}\right)p_g - \left(N_{ww}+\frac{b_w^2}{K_{dr}}\right)P_{wg}\right)\right]_i$$

$$+\delta_t\left[\rho_w\frac{b_w}{K_{dr}}\sigma_v V_b\right]_i - \sum_{j=1}^{n_{\text{face},i}} W_{w,ij}^{n+1} - \left[\rho_w^{n+1}f_w^{n+1}V_b\right]_i \quad i=1,\ldots,n_{\text{elem}}. \tag{67}$$

The global residual vectors are obtained by assembly of the element residual vectors:
$\boldsymbol{R}_g = [R_{g,1},\ldots,R_{g,n_{\text{elem}}}]^T$, $\boldsymbol{R}_w = [R_{w,1},\ldots,R_{w,n_{\text{elem}}}]^T$. In vector form, the system of $n_{\text{phase}} n_{\text{elem}}$ algebraic equations of the flow problem reads

$$\begin{bmatrix} \boldsymbol{R}_g \\ \boldsymbol{R}_w \end{bmatrix}^{n+1} = \begin{bmatrix} \boldsymbol{0} \\ \boldsymbol{0} \end{bmatrix}, \tag{68}$$

which must be solved at every time step for the vector of element gas-phase pressures
$\boldsymbol{P}_g^{n+1} = [p_{g,1}^{n+1},\ldots,p_{g,n_{\text{elem}}}^{n+1}]^T$, and the vector of element water-phase saturations $\boldsymbol{S}_w^{n+1} = [S_{w,1}^{n+1},\ldots,S_{w,n_{\text{elem}}}^{n+1}]^T$. The water phase pressure is determined with the help of the capillary pressure relation (equation (20)), and the gas saturation is determined from the constraint $S_g + S_w \equiv 1$.

The mechanics problem (65) and the flow problem (68) are coupled through the inverse Biot modulus $\boldsymbol{N}$, the drained bulk modulus K_{dr}, the Biot coefficient $\boldsymbol{b}$, and the bulk density ρ_b. Further, $\boldsymbol{N}$, $\boldsymbol{b}$, and ρ_b are themselves functions of fluid pressures, saturations, and solid displacements.

4. Solution Strategy

In this section, we discuss our scheme for solving the coupled system (equations (65–68)). We use a sequential-implicit solution scheme [*Park*, 1983; *Zienkiewicz et al.*, 1988; *Armero and Simo*, 1992; *Armero*, 1999; *Jha and Juanes*, 2007; *Kim et al.*, 2011c] to solve the coupled multiphase and geomechanics problem. In this scheme, the two subproblems of multiphase flow and mechanics are solved in sequence such that each subproblem is solved using implicit time discretization. An outer iteration is performed

over the two subproblems to ensure full convergence of the solution at every time step. As opposed to the simultaneous solution approach [*Lewis and Sukirman*, 1993; *Wan et al.*, 2003; *Jeannin et al.*, 2007; *Jha and Juanes*, 2007], where all the unknowns (displacements, pressures, and saturations) are solved for simultaneously at each time step, the sequential iterative approach [*Park*, 1983; *Zienkiewicz et al.*, 1988; *Armero and Simo*, 1992; *Armero*, 1999; *Jha and Juanes*, 2007; *Kim et al.*, 2011c] solves the system separately for the mechanics (displacements, Lagrange multipliers) and the flow (pressures, saturations).

4.1. Mechanics Subproblem

We solve the linear systems of equations of the mechanical problem using Newton's method. Given an approximation $[U^{n+1}, L^{n+1}]^{(k)}$ to the solution at t_{n+1}, an improved solution is obtained as $[U^{n+1}, L^{n+1}]^{(k+1)} = [U^{n+1}, L^{n+1}]^{(k)} + [\delta U^{n+1}, \delta L^{n+1}]^{(k)}$, where the correction vector is the solution to the system of linear equations (removing the explicit reference to the time level $n + 1$):

$$\begin{bmatrix} K & C^T \\ C & 0 \end{bmatrix}^{(k)} \begin{bmatrix} \delta U \\ \delta L \end{bmatrix}^{(k)} = - \begin{bmatrix} R_u \\ R_l \end{bmatrix}^{(k)}, \tag{69}$$

where the block matrices are obtained via element-by-element assembly of the individual nodal contributions to the Jacobian:

$$K_{ab} = \frac{\partial R_{u,a}}{\partial U_b} = \int_\Omega B_a^T D B_b d\Omega, \tag{70}$$

$$C_{ab}^T = \frac{\partial R_{u,a}}{\partial L_{\bar{b}}} = \int_{\Gamma_{f_+}} \eta_a^T \eta_{\bar{b}} d\Gamma - \int_{\Gamma_{f_-}} \eta_a^T \eta_{\bar{b}} d\Gamma. \tag{71}$$

Above, K is the stiffness matrix, which is symmetric positive definite; for linear elasticity in 3-D,

$$D = \frac{E}{(1+v)(1-2v)} \begin{bmatrix} 1-v & v & v & 0 & 0 & 0 \\ v & 1-v & v & 0 & 0 & 0 \\ v & v & 1-v & 0 & 0 & 0 \\ 0 & 0 & 0 & \frac{1}{2}(1-2v) & 0 & 0 \\ 0 & 0 & 0 & 0 & \frac{1}{2}(1-2v) & 0 \\ 0 & 0 & 0 & 0 & 0 & \frac{1}{2}(1-2v) \end{bmatrix}, \tag{72}$$

where E is the Young modulus and v is the Poisson ratio.

Matrix C is the part of the Jacobian associated with the slip constraint (equation (49)) and consists of direction cosine matrices to convert from the global coordinate system to the fault coordinate system (vice versa for C^T). Note that for a linear elastic material with time-independent material properties and boundary conditions, the Jacobian matrix does not change with time, although the residuals may change due to coupling with the flow and due to fault slip.

To visualize the fault contribution to the linear system, we can write equation (69) as

$$\begin{bmatrix} K_{rr} & K_{r+} & K_{r-} & 0 \\ K_{+r} & K_{++} & 0 & C_+^T \\ K_{-r} & 0 & K_{--} & -C_-^T \\ 0 & C_+ & -C_- & 0 \end{bmatrix}^{(k)} \begin{bmatrix} \delta U_r \\ \delta U_+ \\ \delta U_- \\ \delta L \end{bmatrix}^{(k)} = - \begin{bmatrix} R_{u,r} \\ R_{u,+} \\ R_{u,-} \\ R_l \end{bmatrix}^{(k)}, \tag{73}$$

where the top row corresponds to displacement nodes excluding the fault positive and negative side nodes, and the individual entries of the rotation matrices are

$$C_{a_+\bar{b}} = \int_{\Gamma_{f_+}} \eta_a^T \eta_{\bar{b}} \, d\Gamma, \tag{74}$$

$$C_{a_-\bar{b}} = \int_{\Gamma_{f_-}} \eta_a^T \eta_{\bar{b}} \, d\Gamma. \tag{75}$$

The fault slip global vector D is either prescribed as part of the fault definition, or if a constitutive model for fault friction is given, it is computed dynamically from equation (52). In the latter case, the mechanics problem is nonlinear because fault slip is a function of the fault tractions (the Lagrange multipliers), which are limited by the fault constitutive model and depend on the slip. Hence, an iterative scheme is employed to solve the mechanics problem in the case of dynamic slip evolution. The algorithm is as follows [*Aagaard et al.*, 2013]:

1. Solve equation (73) to determine the Lagrange multipliers, $L^{(k)}$, and the displacements, $U_r^{(k)}$, $U_+^{(k)}$, and $U_-^{(k)}$, corresponding to the current estimate of slip, $D^{(k)}$. Compute tractions on the fault. If $\tau > \tau_f$, or if $\tau < \tau_f$ but the iteration has not converged due to overshoot in slip from the previous iteration, compute the perturbation in the Lagrange multipliers, $\delta L^{(k*)}$, necessary to satisfy the fault constitutive model for the current estimate of slip as follows:

$$\delta L_{\bar{a},i}^{(k*)} = (1 - \delta_{i,n_{\dim}}) L_{\bar{a},i}^{(k)} \left(\frac{\tau_{f,\bar{a}}^{(k)} - \tau_{\bar{a}}^{(k)}}{\tau_{\bar{a}}^{(k)}} \right),$$
$$1 \leq i \leq n_{\dim}, \ \forall \bar{a} = 1, \ldots, n_{f,\text{node}}, \tag{76}$$

where $(k*)$ denotes perturbation to the kth iteration, and $\delta_{i,n_{\dim}}$ is the Kronecker's delta function ensuring that only the shear components of the Lagrange multiplier are perturbed.

2. Compute the displacement increments on the fault positive and negative sides, $\delta U_+^{(k*)}$ and $\delta U_-^{(k*)}$, corresponding to the perturbation $\delta L^{(k*)}$, while assuming that the deformation due to slip is localized to the fault positive and negative side nodes only, i.e., $\delta U_r^{(k*)} = 0$. This is accomplished by solving two linear subsystems, extracted from equation (73), for the respective side nodes,

$$K_{++} \delta U_+^{(k*)} = -C_+^T \delta L^{(k*)},$$
$$K_{--} \delta U_-^{(k*)} = C_-^T \delta L^{(k*)}, \tag{77}$$

where the bulk deformation term, the body weight term, and the boundary traction term from equation (63) do not appear because they are assumed fixed during this step.

3. Update the fault slip

$$\delta D^{(k)} = C(\delta U_+^{(k*)} - \delta U_-^{(k*)}). \tag{78}$$

Since the change in slip may lead to a change in the friction stress at the slipping nodes (e.g., in slip-weakening and rate- and state-dependent models), the perturbation calculation above can be further optimized by iterating over equations (76–78) in an inner loop [*Aagaard et al.*, 2013]. The slip vector for the next iteration is $D^{(k+1)} = D^{(k)} + \delta D^{(k)}$.

4.2. Multiphase Flow Subproblem
We solve the linear system of equations of the multiphase flow problem using Newton's method. The correction vector is the solution of the linear system of equations:

$$\begin{bmatrix} \dfrac{\partial R_g}{\partial P_g} & \dfrac{\partial R_g}{\partial S_w} \\[2mm] \dfrac{\partial R_w}{\partial P_g} & \dfrac{\partial R_w}{\partial S_w} \end{bmatrix}^{(k)} \begin{bmatrix} \delta P_g \\ \delta S_w \end{bmatrix}^{(k)} = - \begin{bmatrix} R_g \\ R_w \end{bmatrix}^{(k)}, \tag{79}$$

where the partial derivatives of the residuals are evaluated using the constitutive equations (equations (29) and (31)) that relate rock and fluid properties to the fluid pressures and saturations.

4.3. Fixed-Stress Sequential Method

In this work, we use the fixed-stress sequential iterative method [*Kim et al.*, 2011b] to solve the coupled multiphase geomechanics problem. In this method, the flow subproblem is solved first keeping the rate of the volumetric total stress fixed, then the mechanics subproblem is solved keeping the fluid pressures and the saturations fixed:

$$\begin{bmatrix} U^n \\ L^n \\ P_g^n \\ S_w^n \end{bmatrix} \xrightarrow{\mathcal{A}^{\text{flow}}} \begin{bmatrix} U^* \\ L^* \\ P_g^{n+1} \\ S_w^{n+1} \end{bmatrix} \xrightarrow{\mathcal{A}^{\text{mech}}} \begin{bmatrix} U^{n+1} \\ L^{n+1} \\ P_g^{n+1} \\ S_w^{n+1} \end{bmatrix}, \tag{80}$$

where $\mathcal{A}^{\text{flow}} : R_w=0, R_g=0, \delta_t\sigma_v=\text{prescribed}$, is the multiphase flow subproblem with fixed rate of volumetric total stress, and $\mathcal{A}^{\text{mech}} : R_u=0, R_l=0, P_g, S_w=\text{prescribed}$, is the mechanics subproblem with fixed flow variables. Superscript * indicates intermediate solution. The volumetric total stress, σ_v, appears in the accumulation term of the multiphase flow equations (equations (66) and (67)). To keep the rate of σ_v fixed during the flow solve, this term is evaluated explicitly using the value of $\delta_t\sigma_v$ from the previous sequential iteration.

This sequential procedure is iterated at each time step until convergence of the full solution. Recently, it has been shown that the fixed-stress operator split is unconditionally stable, and it enjoys excellent convergence properties compared with the other unconditionally stable sequential iterative method (the undrained split) [*Kim et al.*, 2011b, 2011c, 2013].

5. Implementation

We developed a coupled multiphase flow and geomechanical simulator by coupling Stanford's General Purpose Research Simulator (GPRS) [*Cao*, 2002; *Pan and Cao*, 2010] as the flow simulator, and PyLith [*Aagaard et al.*, 2012, 2013] as the mechanics simulator. Below we describe the major steps in the development of this coupled simulator.

5.1. The Flow Simulator

GPRS is a general purpose, object-oriented, reservoir simulator for multiphase/multicomponent subsurface flows. It treats element connections through a general connection list, which allows for both structured and unstructured grids. GPRS is capable of handling complex production and injection scenarios in the field, such as wells perforated at multiple depths and flowing under variable rate and pressure controls. The original simulator [*Cao*, 2002; *Pan and Cao*, 2010] does not account for coupling with the mechanical deformation, and it models the mechanical behavior of the system through a user-provided *rock compressibility* [*Aziz and Settari*, 1979]. We modified and extended the original code to implement the coupling with the mechanics simulator. In particular, we implemented the functionality to compute the modified accumulation term in the fluid phase mass balance equations (equations (66) and (67)). We also modified the setup of the linear system to implement the flow step of the fixed-stress sequential solution scheme (equation (80)).

5.2. The Mechanics Simulator

PyLith is a finite element code for the simulation of static and dynamic large-scale deformation problems [*Aagaard et al.*, 2012, 2013]. Much of its development has been motivated by the modeling of earthquake physics; however, its applicability extends to problems at any other scale, such as the reservoir scale or the laboratory scale. Some of the advantages of PyLith are (1) it is an open-source code and can be modified for specific purposes; (2) it is written using C++ and Python languages and is extendable; (3) it is suitable for parallel computing; (4) it allows localized deformation along discrete features, such as faults; and (5) it is well integrated with meshing codes, such as LaGriT for tetrahedral meshes [*LaGriT*, 2013] and CUBIT for both tetrahedral and hexahedral meshes [*CUBIT*, 2013]. PyLith uses an implicit formulation to solve quasi-static problems and an explicit formulation to solve dynamic rupture problems. Originally, PyLith is not coupled to any fluid flow model. We modified the code of PyLith version 1.8.0 and coupled it with the flow

simulator, GPRS. In particular, we implemented a C++ class, *iGPRS*, to allow communication between the flow and the mechanics simulators. *iGPRS* provides the functionality required for exchanging information (pressures, saturations, and volumetric total stress) between the two simulators.

PyLith supports distributed memory parallelization (Message Passing Interface or MPI) whereas GPRS's parallelization is based on the shared memory architecture (Multiprocessing or OpenMP). We integrated the two such that we can run the coupled simulator on a cluster with multiple compute nodes (distributed memory) where individual nodes have multiple cores or processors (shared memory).

5.3. Grid

We use a single grid for both GPRS and PyLith. The grid is generated using CUBIT [*CUBIT*, 2013] or LaGriT [*LaGriT*, 2013] mesh generation software. We define geologic surfaces, material regions, faults, and pinch-outs during the geometry creation stage. Then we mesh the domain with hexahedral elements using a fine mesh in the reservoir domain and an increasingly coarse mesh in the overburden, underburden, and sideburden regions. We export the grid in a finite element format such as the Exodus-II format [*CUBIT*, 2013] for PyLith. We process the grid file using a MATLAB script to generate the equivalent finite volume grid in the domain with element centroid coordinates, element bulk volumes, and face transmissibilities in the Corner Point Geometry format [*Schlumberger*, 2009]. Any grid elements lying outside the flow region of interest (e.g., in overburden and underburden; see section 2.5) are deactivated for the solution of the flow problem. GPRS uses the finite volume grid for simulating flow in the region of interest. The two simulators exchange pressures, saturations, and volumetric stress information inside this region.

5.4. Implementation of Faults

To support relative motion across fault surfaces, PyLith modifies the grid topology to create zero-thickness fault elements and adds additional degrees of freedom to hold the Lagrange multipliers and fault slip vectors at the Lagrange nodes [*Aagaard et al.*, 2012, 2013] (Figures 1 and 2). PyLith solves the contact problem iteratively in two steps (section 4.1). In the first step, the elasticity problem is solved over the entire domain to update the displacements and the fault tractions (Lagrange multipliers) corresponding to the current estimate of the slip (equation (73)). The Lagrange multipliers are compared with the friction stress on the fault and are adjusted to be compatible with the fault constitutive model. In the second step, the fault slip is updated corresponding to the adjustment in the Lagrange multipliers while assuming that the deformation due to slip is localized to the elements adjacent to the fault, that is, that displacements at nonfault nodes do not change from their values at the current Newton iteration (equation (77)). If the fault slips over the entire domain, such that the assumption of deformation being limited to the adjacent elements is not met, the convergence of the iterative scheme is poor. Also, if the fault friction coefficient changes significantly with slip (e.g., in rate- and state-dependent models; equation (37)), it leads to large changes in $\tau_{f,\bar{a}}$ (equation (76)) at every iteration and convergence may degrade. To improve convergence, a line-search routine is used as part of the iterative scheme to find the optimum perturbation in the Lagrange multipliers that minimizes the combined mismatch between the fault friction and the fault shear traction at all the fault nodes [*Aagaard et al.*, 2013]. We modified PyLith's original line-search routine such that the inequality constraint, $\tau \leq \tau_f$, is always honored.

5.5. Initialization

The flow simulation is initialized under the assumption of vertical equilibrium (section 2.5) with the initial pressure and saturation fields calculated using the rock and fluid properties (depth, fluid density, capillary pressure, and fluid contacts). PyLith is initialized with the initial displacement field obtained from an elastic prestep calculation using initial and boundary displacements and stresses. Initial stresses and boundary tractions are total stresses calculated with bulk densities that account for any fluid contact in the flow domain.

5.6. Linear Solver

The mechanics problem (equation (69)) leads to a saddle-point problem due to the use of Lagrange multipliers to implement the fault slip constraint. Custom preconditioners are required to solve the linear system efficiently. We solve equation (69) using the Portable, Extensible Toolkit for Scientific Computation (PETSc) [*Balay et al.*, 1997] multigrid preconditioner for the elasticity submatrix in conjunction with a custom fault
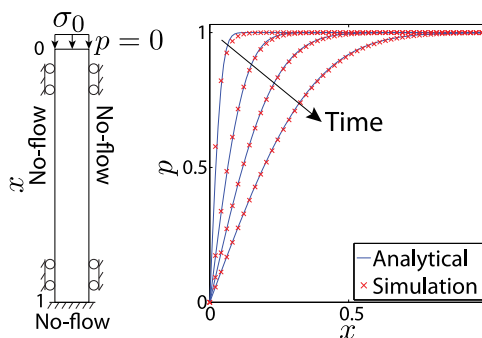
Figure 4. Terzaghi's uniaxial compaction problem. (left) Model with boundary conditions. (right) Comparison of pressure evolutions from the numerical simulation and the analytical solution. The dimensionless pressure is plotted against dimensionless distance at four different times.

preconditioner for the Lagrange multiplier submatrix [*Aagaard et al.*, 2013, 2012]. We solve the flow problem (equation (79)) using the SAMG multigrid preconditioner [*SAMG*, 2010; *Pan and Cao*, 2010].

6. Representative Numerical Simulations

We illustrate the validity and applicability of our modeling approach through a number of representative simulations. Some are verification problems and others are more realistic scenarios. We conduct these simulations using our coupled simulator. The 2-D numerical example simulations are conducted with a 2-D implementation in plane strain. Note that both GPRS and PyLith have been tested previously on respective benchmark problems, i.e., validation on flow-only problems for GPRS [*Cao*, 2002] and mechanics-only problems for PyLith [*Aagaard et al.*, 2012]. Fault implementation in PyLith has been validated by comparison with analytical solutions from elastic dislocation theory [*Okada*, 1992].

6.1. The Terzaghi Problem

Our first example is a uniaxial compaction test under drained conditions, also known as Terzaghi's problem [*Terzaghi et al.*, 1996; *Wang*, 2000]. The purpose of Terzaghi's problem is to test the accuracy of the numerical code for fluid-to-solid coupling. The model problem is a laterally constrained specimen, subjected to a uniform compressive traction applied suddenly at the top surface (Figure 4a). All sides of the specimen are no-flux boundaries except the top surface, which is open to flow. At $t = 0^+$, the specimen compacts and the pore pressure rises to its undrained value because of the sudden application of the load, also known as the Skempton effect [*Skempton*, 1954]. The undrained values of pressure and total stress serve as the initial condition for the drained part of the consolidation process. As time increases, the specimen consolidates vertically as the fluid leaks out from the top permeable surface. It is a one-dimensional problem with a constant total stress. Under these conditions, diffusion of pore pressure decouples from stress and satisfies a homogeneous diffusion equation with known analytical solution [*Wang*, 2000]. Strain due to compaction is proportional to the pressure drop.

We used the following values of the relevant parameters: length of 50 m, compression of 2.125 MPa, Young modulus of 120 MPa, drained Poisson ratio of 0.3, Biot coefficient of 1.0, porosity of 0.2, and hydraulic diffusivity of 1.9×10^{-6} m²/s. Our numerical simulation agrees well with the analytical solution (Figure 4b).

6.2. The Mandel Problem

Mandel's problem [*Mandel*, 1953; *Abousleiman et al.*, 1996] has been used as a benchmark problem for testing the validity of numerical codes of coupled poroelasticity. Its main feature, the Mandel-Cryer
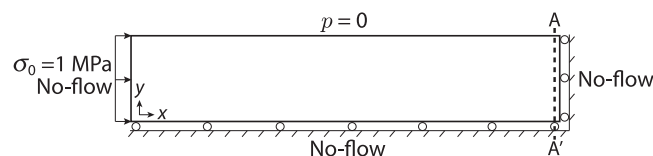

Figure 5. Mandel's problem. The model dimensions are $L_x \times L_y \times L_z = 50 \times 10 \times 0.5$ m, discretized with $100 \times 20 \times 1$ hexahedral cells. A uniform and constant compression of 1 MPa is applied on the left boundary while the right and bottom boundaries are fixed in the normal direction. The top boundary is traction-free. For the flow model, the top boundary is a drained boundary with constant pressure $p = 0$, and the other three boundaries are no-flow boundaries.

effect, is that the pore pressure at the center of a loaded specimen rises above its initial value because of the two-way coupling between fluid flow and solid deformation. Mandel's problem involves a long specimen of rectangular cross section pressed on one side with an impermeable plate that applies a constant compressive stress σ_0 and fixed on two sides using impermeable roller boundaries (Figure 5).
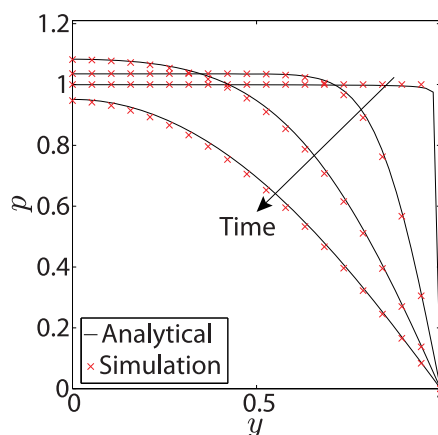
Figure 6. Comparison of the pressure evolution from the analytical solution and from the numerical simulation for the Mandel problem. The pressure is plotted along the AA′ line shown in Figure 5. Pressure is nondimensionalized with the applied compressive stress, and distance is nondimensionalized with the width L_y. Note that, near $y = 0$, the pressure increases at early times in accordance with the Mandel-Cryer effect before beginning to decrease.

The fourth side of the cross section is free from normal and shear stresses (traction-free boundary) and is open to the atmosphere (constant pressure boundary). The porous medium is saturated with a slightly compressible fluid, water, with initial pressure set at the reference value, $p_0 = 0$. Since the specimen is long, we assume plane strain conditions, namely, that the displacement and fluid flux vanish in the z direction (perpendicular to the 2-D domain).

With these boundary conditions, the three-dimensional equations of poroelasticity reduce to one-dimensional equations for $\sigma_{xx}(y,t)$ and $p(y,t)$, which can be solved analytically [*Mandel*, 1953; *Abousleiman et al.*, 1996]. At $t = 0^+$, a uniform undrained pressure is generated by the Skempton effect, along with uniform stress $\sigma_{xx} = -\sigma_0$. The specimen expands toward the top boundary due to the Poisson effect. As time progresses, the pressure near the top boundary decreases because of fluid drainage, which makes the specimen more compliant there. If the hydraulic diffusivity is small, the effect of drainage is not observed immediately near the no-flux bottom boundary. This results into load transfer of compressive total stress toward the bottom boundary, in response to which the pressure there continues to rise above its undrained value. At long times, all excess pressure vanishes and a uniform horizontal stress, $\sigma_{xx} = -\sigma_0$, returns. Hence, the pressure evolution at points away from the drained boundary is nonmonotonic, a phenomenon not observed in a purely diffusive process such as that modeled by the Terzaghi theory, where the pressure is uncoupled from the solid deformation.

For our example, we choose a Young modulus of 18 GPa, drained Poisson ratio of 0.25, undrained Poisson ratio of 0.49, reference porosity of 0.05, and hydraulic diffusivity of 2.2×10^{-7} m²/s. Figure 6 compares the pressure from the analytical solution and the numerical simulation along the width of the specimen near the right boundary at different times. Notice the increase in pressure near $y = 0$ at early times, which illustrates the Mandel-Cryer effect.
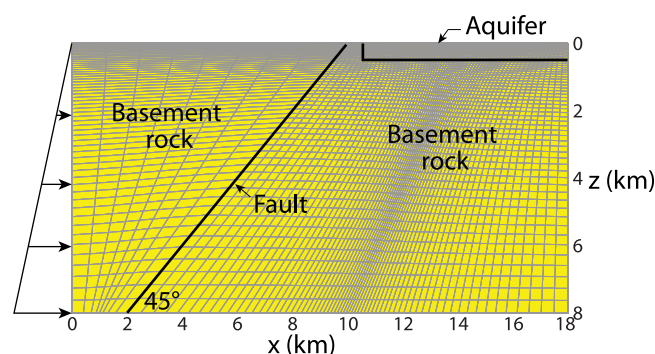
6.3. Effect of Groundwater Pumping on Fault Stability

This example illustrates the role of coupling between flow and deformation in determining the stability of faults. We model groundwater pumping from an unconfined aquifer, resulting in a drop in the water table and accompanying changes in poroelastic stresses in and around the aquifer. The stability of a nearby fault is affected due to changes in stress resulting from unloading of the crust in a poroelastic medium. We model this problem in a 2-D plane strain domain with a reverse fault and an aquifer (Figure 7). The aquifer is 500 m thick and 7.5 km wide. The fault dips at 45° and strikes at a distance of
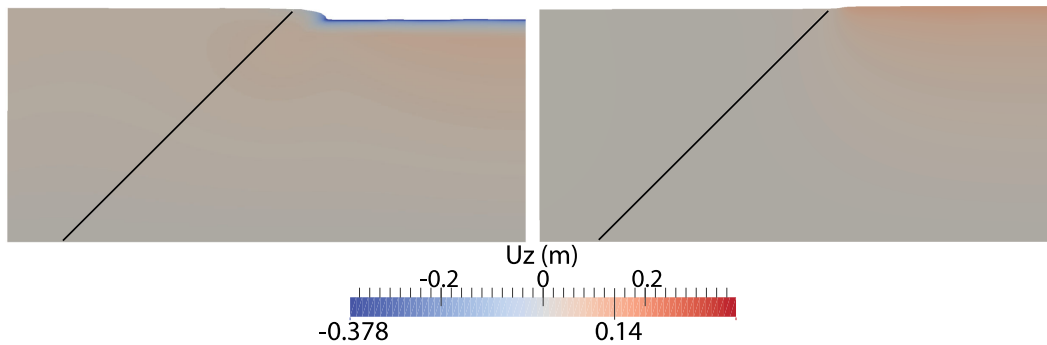

Figure 7. Plane strain model with an aquifer and a fault to investigate the effect of groundwater pumping on fault stability. A lithostatic overburden and a lateral compression at twice the lithostatic gradient create reverse faulting conditions. Permeability is high in the aquifer and very low in the basement rock. The domain is discretized with a finer mesh near the surface to simulate a drop in water table.

Figure 8. Vertical displacement field from (left) coupled and (right) uncoupled simulations. The displacement field magnified by a factor of 1000.

500 m from the aquifer. To produce a uniform drop in water table and a confined unloading of the crust, we assume that permeability is low everywhere except in the aquifer. The fault is located in the low-permeability region and is impermeable. We simulate the problem using both coupled and uncoupled approaches to highlight the role of poroelastic coupling. In the coupled approach, we simulate a drop in water table due to pumping from the aquifer over a period of 50 years. Pressure depletion in the aquifer also results in compaction of the aquifer and subsidence at the ground surface. In the uncoupled approach, the mechanics problem is solved independently of the flow with an instantaneous load corresponding to the mass of water removed from groundwater pumping. We simulate this unloading by decreasing the aquifer bulk density from $\rho_b = \phi \rho_w + (1-\phi)\rho_s$ to $\rho_b = \phi \rho_g + (1-\phi)\rho_s$ in the layers known to be depleted from the coupled simulation. We use initial values of porosity and density to calculate ρ_b in the uncoupled simulation. The uncoupled approach treats the poroelastic medium as an equivalent purely elastic medium.

Initially, the stress distribution is lithostatic, and the pressure distribution is hydrostatic corresponding to a water saturated medium. Compression at twice the lithostatic gradient is applied on the $x = 0$ boundary, the top boundary is traction-free, and normal displacement at the other two boundaries are fixed to zero. A no-flow boundary condition is imposed on all four boundaries. The unconfined behavior of the aquifer is modeled by placing "air injectors" in the top row of cells in the aquifer, which maintain a constant pressure equal to atmospheric in these cells by injecting air as water is withdrawn.

The rock and fluid properties are as follows: the Young modulus increases linearly with depth from 100 MPa at $z = 1$ m to 64 GPa at $z = 8$ km, the Poisson ratio is 0.25, the Biot coefficient is 1, and the porosity is uniform and equal to 0.1. The permeability in the aquifer decreases exponentially with depth as $k(z) = k_{max} \exp(-az)$, where we choose $k_{max} = 5000$ md and $a = 0.015$ m^{-1}. The permeability outside the aquifer is 0.0001 md. The relative permeabilities are modeled using Corey-type relations [*Lomeland et al.*, 2005] as $k_{rw} = S_n^{L_w}/(S_n^{L_w} + E_w(1-S_n)^{T_w})$, $k_{rg} = (1-S_n)^{L_g}/((1-S_n)^{L_g} + E_g S_n^{T_g})$, where the normalized water saturation is $S_n = (S_w - S_{wl})/(1 - S_{wl} - S_{gl})$. We choose the irreducible water saturation $S_{wl} = 0.001$ and the residual gas saturation $S_{gl} = 0$. We choose the empirical constants as $L_w = 0.8$, $E_w = 3$, $T_w = 4$, and $L_g = 1.9$, $E_g = 4$, $T_g = 1.1$. We fix the capillary pressure to zero. The rock density is $\rho_s = 2600$ kg/m^3. At surface conditions, fluid densities are $\rho_w = 1000$ kg/m^3 and $\rho_g = 1.2$ kg/m^3, and dynamic viscosities are $\mu_w = 1$ cp and $\mu_g = 0.001$ cp. Water compressibility is assumed to be constant, $c_w = 8.64 \times 10^{-5}$ MPa^{-1}. Note that the air pressure is always close to atmospheric because of the unconfined nature of the aquifer. The water withdrawal rate is fixed at 0.0957 kg/s/m equally distributed among eight
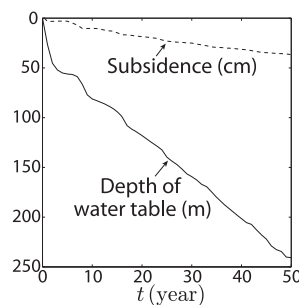

Figure 9. Evolution of water table and surface subsidence from the coupled simulation. The values are averaged over the aquifer area.
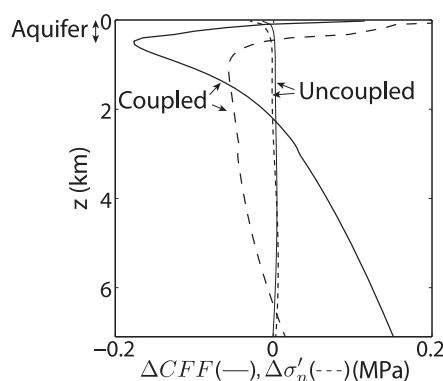
Figure 10. Depth profiles of the change in Coulomb Failure Function ΔCFF and the change in effective normal traction $\Delta\sigma'_n$ on the fault from both the coupled and uncoupled simulations. Changes are due to groundwater pumping from the aquifer.

producers. The fault friction coefficient is $\mu_f = 0.5$, and it stays constant because we do not induce slip for the prescribed properties and amount of water withdrawal. Instead, we evaluate the impact of groundwater pumping on fault stability by computing the change in the Coulomb Failure Function, $\Delta CFF = \Delta|\tau| + \mu_f \Delta\sigma'_n$, on the fault [*Reasenberg and Simpson*, 1992].

Displacements are very small everywhere except in the aquifer, where the effects of elastic loading are substantial: compaction in the coupled simulation, and expansion the uncoupled simulation (Figure 8). In the coupled simulation, the water table in the aquifer drops to 240 m (averaged over the aquifer), and the accompanying subsidence is 0.38 m (Figure 9). In terms of fault stability, up-dip shear on the fault decreases up to a depth $z \approx 1.8$ km because of contraction of the aquifer, and it increases below that depth due to expansion of the basement rock, which is being unloaded. As a result, ΔCFF is negative in the depth interval 90 m $< z <$ 2.3 km, with a minimum at the base of the aquifer, below which it increases monotonically with depth (Figure 10). ΔCFF becomes positive below $z = 2.3$ km, suggesting stabilization of the fault above this depth, and destabilization of the fault below this depth, due to pumping.

In the uncoupled simulation, loading is confined to the top 300 m of the aquifer, which is the region corresponding to a decrease in the bulk density due to the drop in the water table. Compression and shear on the fault increase in this interval such that the fault is stabilized marginally ($\Delta CFF < 0$). Below $z = 300$ m, ΔCFF is positive reaching a maximum of 4200 Pa at $z = 4.2$ km. However, these values are an order of magnitude smaller than those in the coupled case.

Our results show that groundwater pumping can favor fault slip at depth and that stability of the fault cannot be assessed if poroelastic effects are ignored.

6.4. Faulting Due to CO_2 Injection: Plane Strain

This is an example of CO_2 injection in a deep confined aquifer for the purpose of geologic carbon sequestration [*Cappa and Rutqvist*, 2011a]. The aquifer is hydraulic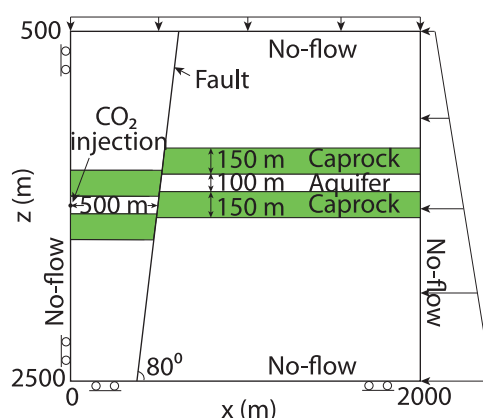ally compartmentalized with a sealing fault that cuts across it. The storage capacity of the aquifer is limited by overpressurization and slip on the fault. As described in *Cappa and Rutqvist* [2011a], we consider a two-dimensional plane strain model with the fault under normal faulting conditions, that is, the vertical principal stress due to gravity is the largest among the three principal stresses (Figure 11). We choose a value of 0.7 for the ratio of horizontal to vertical initial total stress.

CO_2 is injected at a depth of 1500 m in the confined aquifer at a constant rate of 0.01 kg/s/m. We use a slip-weakening model for the fault (equation (36)) in which the coefficient of

Figure 11. Model of the CO_2 injection plane strain case (adapted from *Cappa and Rutqvist* [2011a]). The lateral compression is 0.7 times the overburden, and both increase with the lithostatic gradient. CO_2 is injected in the confined aquifer at a depth of 1500 m. The aquifer is bounded on the top and bottom by a low-permeability caprock, and the fault is impermeable to flow.

Table 1. CO_2 Properties at 40°C

Pressure (MPa)	Density (kg m^{-3})	Viscosity ($\times 10^{-3}$ kg m^{-1} s^{-1})
0.1	1.8	0.0001
8	234	0.0325
10	447	0.0525
12	632	0.0625
16	747	0.0725
20	803	0.0800
30	883	0.0950

friction drops linearly from 0.6 to 0.2 over a critical slip distance of 5 mm [*Cappa and Rutqvist*, 2011a]. The fault cohesion strength is 0 MPa. Permeability and porosity are as follows: 100 md and 0.1 (aquifer), 0.0001 md and 0.01 (caprock), and 10 md and 0.1 (otherwise). The Young modulus and Poisson ratio are 10 GPa and 0.25, respectively. We use a van Genuchten capillary pressure function [*van Genuchten*, 1980], $P_{wg} = p_g - p_w = P_o(\hat{S}^{-1/m} - 1)^{1-m}$, $\hat{S} = (S_w - S_{wlc})/(1 - S_{wlc} - S_{gl})$, where $S_{wlc} = 0.1 S_{wl}$, and P_o is the capillary modulus. We choose the irreducible water saturation $S_{wl} = 0.12$ and the residual gas saturation $S_{gl} = 0.001$. We set $P_o = 5.2$ kPa and $m = 0.4$. We use Corey-type relative permeability functions [*Brooks and Corey*, 1964], $k_{rw} = S_n^L$, $k_{rg} = (1 - S_n)^L$, where S_n is the normalized water saturation defined earlier. We choose an exponent $L = 2$. We have used fluid properties that are representative of water and CO_2 at reservoir conditions [*McCain*, 1990; *Garcia*, 2003; *Juanes et al.*, 2006]. The phase behavior of the system is simplified by the assumption that the two fluids are immiscible. We used a value $\rho_{w,\text{ref}} = 1000$ kg m^{-3} for the density of water at standard conditions, and a constant water compressibility $c_w = 8.64 \times 10^{-5}$ MPa^{-1}. We assumed a constant dynamic viscosity of water $\mu_w = 1.0 \times 10^{-3}$ kg m^{-1}s^{-1}. We relied on the compilation and analysis of [*Garcia*, 2003, chap. 2] for the determination of appropriate CO_2 properties at reservoir conditions. In Table 1, we list the density and dynamic viscosity of CO_2 at 40°C as a function of pressure. Linear interpolation between the table values was used in the simulations.

After 20 days of injection, pressure in the aquifer increases approximately uniformly by 3.6 MPa (Figure 12). Overpressure causes volumetric expansion of the aquifer (Figure 13). This, in turn, results in an increase in the effective normal tractions throughout the aquifer, and an increase in the magnitude of shear tractions at the top and bottom boundaries of the aquifer, namely, at depths of 1450 and 1550 m (Figure 14). There are two interesting observations:

1. The stress evolution (Figure 15a) is such that the bottom of the aquifer at 1550 m reaches the failure line ($\mu_s = 0.6$) first because of the applied traction boundary conditions, which favors normal faulting. Downward slip at the 1550 m depth pulls the 1450 m point down such that the direction of change in the shear traction at 1450 m depth slowly reverses until it also fails by reaching the $\mu_s = 0.6$ failure line.

2. The complete rupture sequence (Figure 15b) is a combination of both seismic and aseismic slips along the fault, with multiple seismic events observed at the bottom boundary of the aquifer.

6.5. Faulting Due to CO_2 Injection: 3-D
This example is similar to the previous one, but here we consider a 4 × 4 × 2 km three-dimensional domain with a 200 m thick anticlinal aquifer (Figure 16), and we use the rate and state-dependent friction model (equation (37)) for the fault friction. The rate and state constitutive parameters are $A = 0.002$, $B = 0.08$, $d_c = 1$ cm, $\mu_0 = 0.4$, and $\tau_c = 0$. These values strongly favor unstable sliding on the fault. Rock and fluid
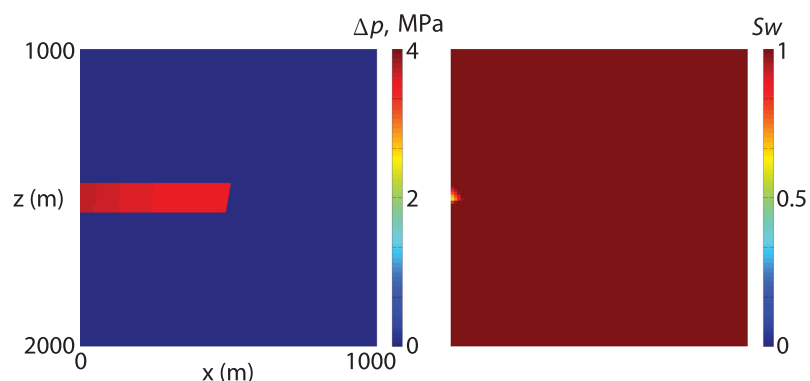
Figure 12. CO_2 injection in the plane strain case. (left) Overpressure and (right) water saturation at $t = 21$ days.
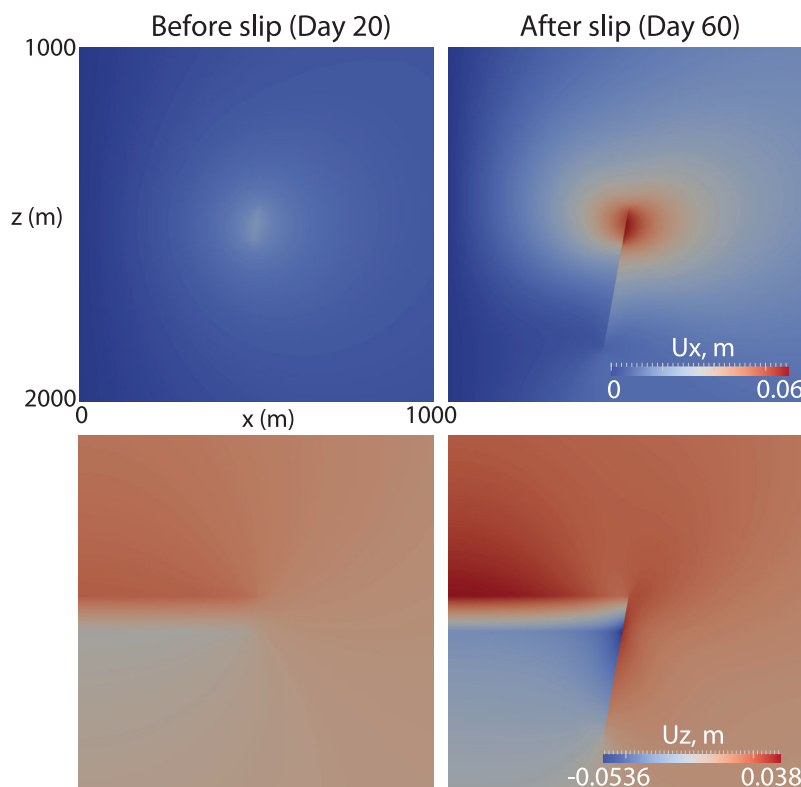
Figure 13. CO_2 injection in the plane strain case. Displacement fields in the horizontal and vertical directions (top row and bottom row, respectively) at two different times: $t = 20$ days (left) and $t = 60$ days (right). Notice the discontinuity in the displacement field across the fault at $t = 60$ days as a result of slip. The rupture propagates along the fault, asymmetrically away from the nucleation point at 1550 m, with the longer part below the nucleation point due to the imposed normal faulting condition. After 60 days, the rupture span along the fault is approximately 400 m.
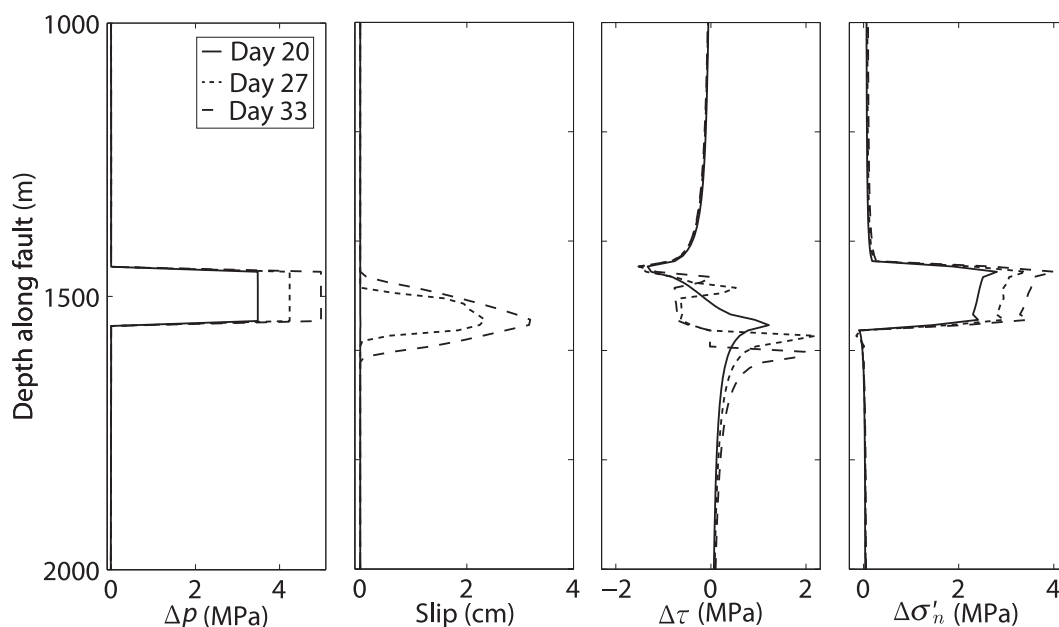
Figure 14. Profiles of overpressure, fault slip, and change in fault tractions plotted along the fault at three different times: day 20 is just before the first slip, and days 27 and 33 are after two other seismic events noted in Figure 15. The overpressure profile nicely outlines the boundaries of the aquifer. The shear traction drops inside the aquifer and increases outside the aquifer, due to slip events near the 1550 m boundary. As points on the fault slip, there is an increase in shear traction at the neighboring nonslipping points, which leads to downward (respectively, upward) movement of the spike in the shear traction below (respectively, above) the aquifer.
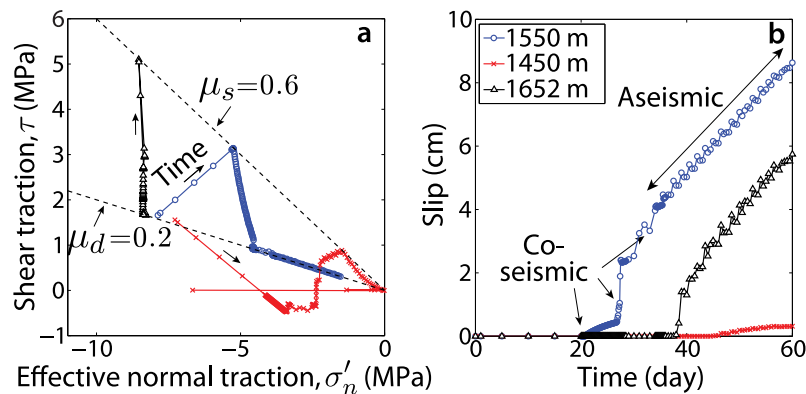
Figure 15. Evolution of (a) stress state and (b) slip on the fault at three depths: bottom of the aquifer (1550 m, blue circles), top of the aquifer (1450 m, red crosses), and below the aquifer in the rupture zone (1652 m, black triangles). At $t = 21$ days, the fault rupture nucleates just underneath the aquifer at 1550 m depth, which reaches the failure criterion ($\mu_s = 0.6$ line) before any other point on the fault. This leads to an increase in shear stresses at points adjacent to 1550 m, which fail in succession. The point at 1652 m depth fails at $t = 38$ days. There is a very small change in the effective normal traction at 1652 m point because there is no overpressure below the aquifer. The top boundary at 1450 m ruptures at $t = 45$ days and relaxes quickly to almost zero shear traction. The three seismic events labeled "coseismic" are analyzed in Figure 14.

properties are identical to the plane strain case above. CO_2 is injected at a rate of 30 million standard cubic feet per day (17.64 kg/s) leading to overpressurization of the aquifer (Figure 17). The anticline is off-centered in y, leading to asymmetry in the overpressure field. Rupture nucleates at the base of the aquifer at $(x, y, z) = (2808, 2850, 1590$ m$)$ after 202 days of injection and propagates on the fault along the bottom boundary of the aquifer. After approximately 2 months, a second rupture sequence begins along the layer just above the base of the aquifer. At $t = 320$ days, the underburden rock layer below the aquifer reaches the failure criterion and slips, and the rupture subsequently propagates in both up-dip and down-dip directions on the fault with higher slip velocity in the down-dip direction (Figure 18). Downward slip is favored due to the imposed normal faulting condition. In Figure 19, we show the evolution of slip and traction on the fault at three points directly under the anticline: base of the aquifer, top of the aquifer, and below the aquifer in the underburden rock. The slip velocity at the base is small and initially constant, resulting in stable sliding; then, it increases sharply due to slip-weakening before decreasing again back to a new stable sliding value that is higher than the earlier one.
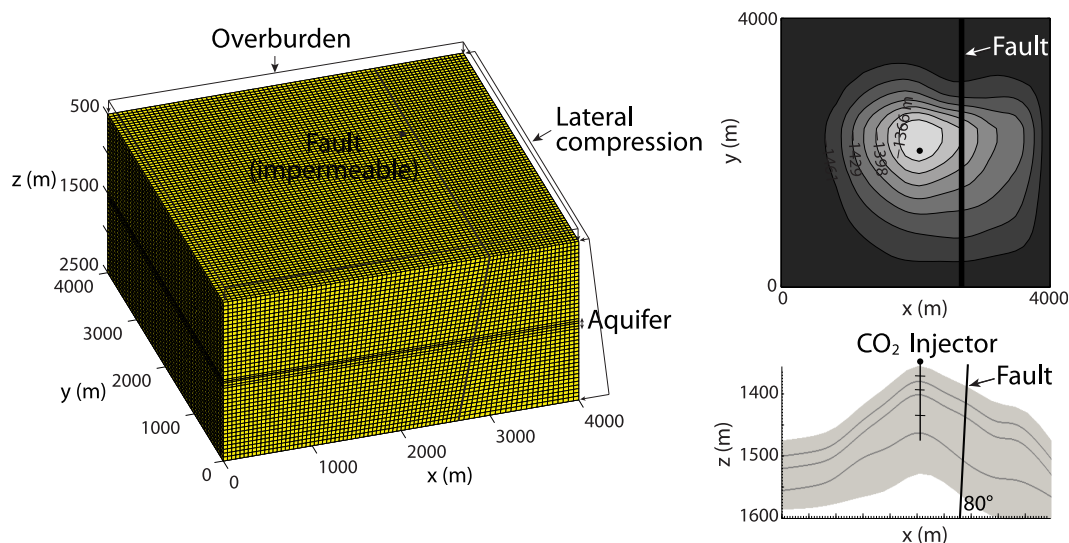

Figure 16. CO_2 injection in a 3-D anticlinal aquifer. (left) The geomechanical domain, shown with the traction boundary conditions on the top and on the right boundaries. The lateral compression is 0.7 times the overburden, and both increase with the lithostatic gradient. Zero-normal displacement is imposed on all other boundaries. A no-flow boundary condition is imposed on all the boundaries. The flow domain is composed of the four layers marked as *aquifer*, and the injector is located near the center of the anticline. (top right) Plan view and (bottom right) cross-section view of the aquifer. Depth contours are marked in the plan view. The cross-section view is exaggerated in the vertical direction.
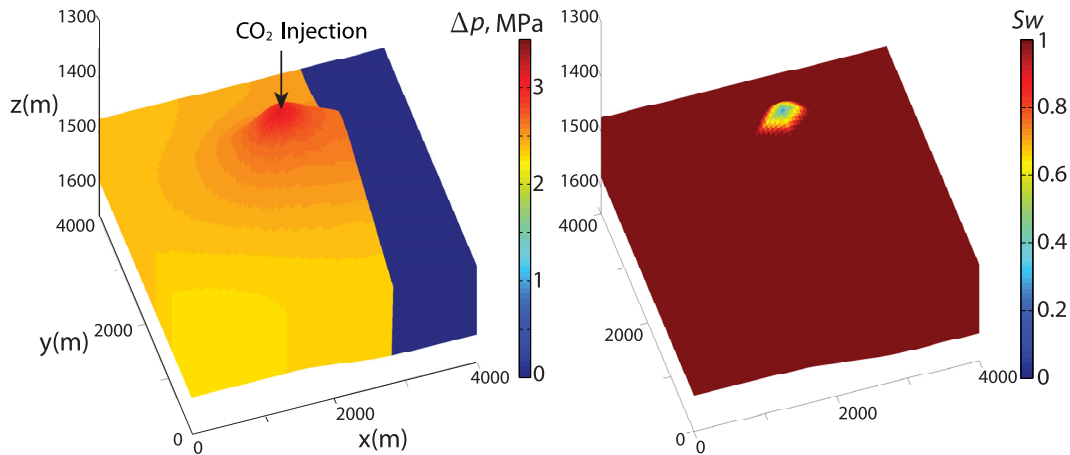
Figure 17. CO_2 injection in a 3-D anticlinal aquifer. (left) Overpressure and (right) water saturation in the aquifer layers at $t = 202$ days, when fault slip starts.

Since the fault is represented as a two-dimensional surface, we can estimate the magnitude of the earthquake from the actual rupture area. Note that since this is a quasi-static simulation with very small slip velocities, earthquake here refers to the seismic event producing an equivalent amount of slip. The earthquake magnitude is given by the expression $M_w = \frac{2}{3}\log_{10}M_0 - 6.0$, where the seismic moment is $M_0 = \int_{\Gamma_f} G|\boldsymbol{d}|d\Gamma$, $|\boldsymbol{d}|$ is the magnitude of the final slip vector at the end of the earthquake, and G is the shear modulus [*Hanks and Kanamori*, 1979]. Assigning the total slip at $t = 400$ days from our simulation to a single seismic event, we obtain an *upper bound* estimate of $M_w = 3.4$ for the earthquake magnitude.
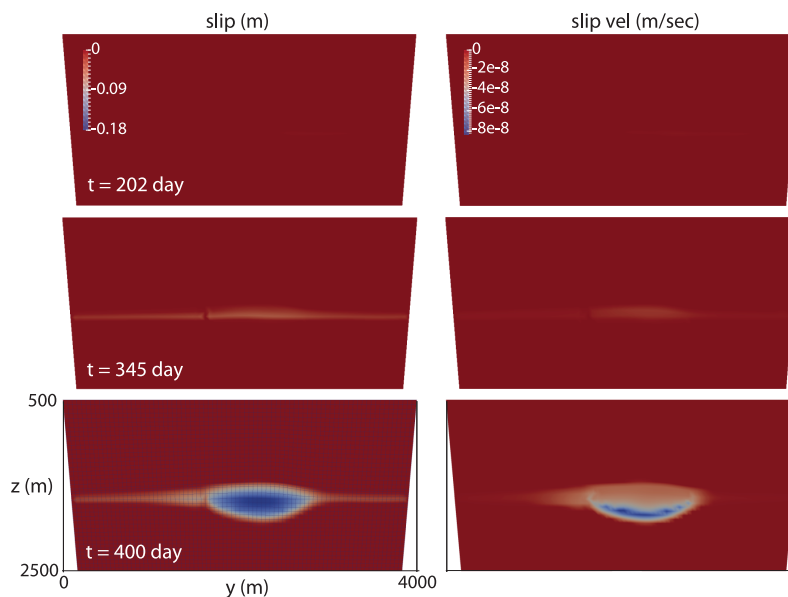

Figure 18. CO_2 injection in a 3-D anticlinal aquifer. Snapshots of (left) slip magnitude and (right) slip velocity on the fault plane at three different times: $t = 202$, 345, and 400 days. The rupture initiates at the bottom of the aquifer and progresses both downward and upward with faster slip velocity downward. The rupture front adopts an ellipsoidal shape following the profile of the aquifer, which is being pressurized. A video that shows the dynamics of fault rupture from the coupled flow-geomechanics simulation is included in the supporting information.
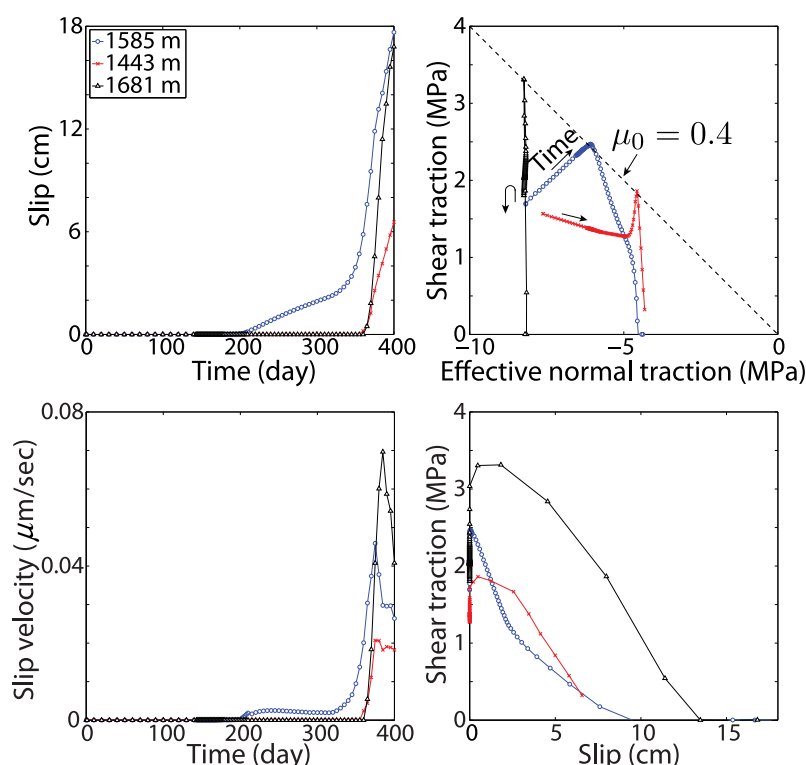
Figure 19. CO_2 injection in a 3-D anticlinal aquifer. Evolution of slip and state of stress on the fault at three depths under the anticline: 1585 m (bottom of the aquifer), 1443 m (top layer of the aquifer), and 1681 m (below the aquifer in the underburden). Slip, slip velocity, and shear traction are in the down-dip direction along the fault.

7. Conclusions

We have presented a new computational model to simulate the coupling between multiphase flow and poromechanics of faults and developed a two-way coupled simulator that interlaces a geomechanics simulator (PyLith) with a multiphase flow simulator (GPRS). Our approach enjoys the following features:

1. It is computationally efficient because it relies on a sequential solution of the two-way coupled problem.

2. It is unconditionally stable, due to the use of the fixed-stress sequential split between multiphase flow and deformation. The model accounts rigorously for multiphase flow effects through a fully nonlinear poromechanics formulation.

3. It represents faults as surfaces embedded in a three-dimensional domain, therefore allowing for a discontinuous displacement field across the fault (fault slip). Our approach elucidates the role of the pressure discontinuity across the fault on the stability of the fault through the definition of a "fault pressure."

4. It incorporates realistic fault constitutive behavior, such as the rate- and state-dependent friction model, capable of simulating runaway fault slip typical of earthquakes.

We assume quasi-static mechanical deformation by neglecting the inertial term in the solid momentum balance equation, and we use an implicit time-marching scheme for the coupled simulation. While this is an excellent approximation prior to fault rupture, during fault slip the inertial term is not negligible due to propagation of seismic waves. We are currently extending the capabilities of our simulation tool to implement a dynamic implicit-explicit time-marching scheme that can take small time steps required to resolve the propagation of rupture on the fault, while taking orders of magnitude larger time steps during aseismic periods.

In order to model leakage from geologic formations, we are implementing flow along faults. We are also investigating the stability and convergence properties of the fixed-stress sequential solution scheme in the presence of faults, especially with slip-weakening.

Our framework allows us to investigate fault slip and induced seismicity in underground reservoirs due to the coupled processes of fluid flow and mechanical deformation, such as those encountered during groundwater withdrawal and geologic CO_2 storage. In this work, we have demonstrated the effectiveness and applicability of our approach through a few synthetic, but realistic, examples. We are currently applying our computational model for the study of ground deformations detected from geodetic measurements via GPS and InSAR [*Hager et al.*, 1991; *Feigl et al.*, 1993; *Teatini et al.*, 2011] and for the post mortem analysis of natural or induced earthquakes [*Gonzalez et al.*, 2012; *van der Elst et al.*, 2013; *Keranen et al.*, 2013; *Brodsky and Lajoie*, 2013].

References

Aagaard, B., S. Kientz, M. Knepley, L. Strand, and C. Williams (2012), *PyLith User Manual, Version 1.8.0*, Comput. Infrastruct. for Geodyn., Univ. of Calif., Davis, Calif.

Aagaard, B. T., M. G. Knepley, and C. A. Williams (2013), A domain decomposition approach to implementing fault slip in finite-element models of quasi-static and dynamic crustal deformation, *J. Geophys. Res. Solid Earth*, 118, 3059–3079, doi:10.1002/jgrb.50217.

Aavatsmark, I. (2002), An introduction to multipoint flux approximations for quadrilateral grids, *Comput. Geosci.*, 6, 405–432.

Abousleiman, Y., A. H.-D. Cheng, L. Cui, E. Detournay, and J.-C. Roegiers (1996), Mandel's problem revisited, *Geotechnique*, 46, 187–195.

Anderson, E. M. (1951), *The Dynamics of Faulting and Dyke Formation With Application to Britain*, Oliver and Boyd, New York, N. Y.

Armero, F. (1999), Formulation and finite element implementation of a multiplicative model of coupled poro-plasticity at finite strains under fully saturated conditions, *Comput. Methods Appl. Mech. Eng.*, 171, 205–241.

Armero, F., and J. C. Simo (1992), A new unconditionally stable fractional step method for non-linear coupled thermomechanical problems, *Int. J. Numer. Methods Eng.*, 35, 737–766.

Armero, F., and J. C. Simo (1993), A priori stability estimates and unconditionally stable product formula algorithms for nonlinear coupled thermoplasticity, *Int. J. Plasticity*, 9, 749–782.

Aziz, K., and A. Settari (1979), *Petroleum Reservoir Simulation*, Elsevier, London, U. K.

Balay, S., W. D. Gropp, L. C. McInnes, and B. F. Smith (1997), Efficient management of parallelism in object-oriented numerical software libraries, in *Modern Software Tools in Scientific Computing*, pp. 163–202, Birkhauser Press, Basel, Switzerland.

Bear, J. (1972), *Dynamics of Fluids in Porous Media*, John Wiley, New York, N. Y.

Bear, J., and M. Y. Corapcioglu (1981), Mathematical model for regional land subsidence due to water pumping, *Water Resour. Res.*, 17, 937–958.

Beeler, N. M., R. W. Simpson, S. H. Hickman, and D. A. Lockner (2000), Pore fluid pressure, apparent friction, and Coulomb failure, *J. Geophys. Res.*, 105, 25,533–25,542.

Beer, G. (1985), An isoparametric joint/interface element for finite element analysis, *Int. J. Numer. Methods Eng.*, 21, 585–600.

Biot, M. A. (1941), General theory of three-dimensional consolidation, *J. Appl. Phys.*, 12, 155–164.

Birkholzer, J. T., and Q. Zhou (2009), Basin-scale hydrogeologic impacts of CO_2 storage: Capacity and regulatory implications, *Int. J. Greenh. Gas Control*, 3, 745–756.

Bishop, A. W. (1959), The principle of effective stress, *Tekniske Ukeblad*, 39, 859–863.

Bishop, A. W., and G. E. Blight (1963), Some aspects of effective stress in saturated and partly saturated soils, *Geotechnique*, 13, 177–197.

Brezis, H. (2011), *Functional Analysis, Sobolev Spaces and Partial Differential Equations*, Springer, New York, N. Y.

Brodsky, E. E., and L. J. Lajoie (2013), Anthropogenic seismicity rates and operational parameters at the Salton Sea Geothermal Field, *Science*, 341, 543–546.

Brooks, R. H., and A. T. Corey (1964), Hydraulic properties of porous media, *Hydrol. Pap. 3*, pp. 892–898, Colo. State Univ., Fort Collins, Colo.

Caine, J. S., and C. B. Forster (1999), *Faults and Subsurface Fluid Flow in the Shallow Crust, Geophys. Monogr. Ser.*, vol. 113, edited by W. C. Haneberg et al., AGU, Washington, D. C.

Cao, H. (2002), Development of techniques for general purpose simulators, PhD thesis, Stanford Univ., Stanford, Calif.

Cappa, F., and J. Rutqvist (2011a), Impact of CO_2 geological sequestration on the nucleation of earthquakes, *Geophys. Res. Lett.*, 38, L17313, doi:10.1029/2011GL048487.

Cappa, F., and J. Rutqvist (2011b), Modeling of coupled deformation and permeability evolution during fault reactivation induced by deep underground injection of CO_2, *Int. J. Greenh. Gas Control*, 5, 336–346.

Carder, D. S. (1945), Seismic investigations in the Boulder Dam area, 1940–1944, and the influence of reservoir loading on earthquake activity, *Bull. Seismol. Soc. Am.*, 35, 175–192.

Carol, I., A. Gens, and E. E. Alonso (1985), A three dimensional elastoplastic joint element, in *Fundamentals of Rock Joints*, pp. 441–451, Centek, Lulea, Sweden.

Carter, R. D., and G. W. Tracy (1960), An improved method for calculating water influx, *Petrol. Trans.*, AIME, 219, 415–417.

Chester, F. M., J. P. Evans, and R. Biegel (1993), Internal structure and weakening mechanisms of the San Andreas Fault, *J. Geophys. Res.*, 98, 771–786.

Chiaramonte, L., M. D. Zoback, J. Friedmann, and V. Stamp (2008), Seal integrity and feasibility of CO_2 sequestration in the Teapot Dome EOR pilot: Geomechanical site characterization, *Environ. Geol.*, 54(8), 1667–1675.

Coussy, O. (1995), *Mechanics of Porous Continua*, John Wiley, Chichester, U. K.

Coussy, O. (2004), *Poromechanics*, John Wiley, Chichester, U. K.

Coussy, O. (2005), Poromechanics of freezing materials, *J. Mech. Phys. Solids*, 53, 1689–1718.

Coussy, O., R. Eymard, and T. Lassabatére (1998), Constitutive modeling of unsaturated drying deformable materials, *J. Eng. Mech.*, 124(6), 658–557.

Coussy, O., P. Dangla, T. Lassabatére, and V. Baroghel-Bouny (2004), The equivalent pore pressure and the swelling and shrinkage of cement-based materials, *Mater. Struct.*, 37, 15–20.

CUBIT (2013), *CUBIT 13.2 User Documentation*, Sandia Natl. Lab., Albuquerque, N. M.

Cueto-Felgueroso, L., and R. Juanes (2013), Forecasting long-term gas production from shale, *Proc. Natl. Acad. Sci. U. S. A.*, 110, 19,660–19,661.

Dake, L. P. (1978), *Fundamentals of Reservoir Engineering*, Elsevier, Oxford, U. K.

Dean, R. H., X. Gai, C. M. Stone, and S. E. Minkoff (2006), A comparison of techniques for coupling porous flow and geomechanics, *Soc. Pet. Eng. J.*, *11*, 132–140.

Dieterich, J. H. (1979), Modeling of rock friction: 1. Experimental results and constitutive equations, *J. Geophys. Res.*, *84*, 2161–2168.

Dieterich, J. H. (1981), Constitutive properties of faults with simulated gouge, in *Mechanical Behaviour of Crustal Rocks: The Handin Volume, Geophys. Monogr. Ser.*, vol. 24, pp. 108–120, AGU, Washington, D. C.

Ellsworth, W. L. (2013), Injection-induced earthquakes, *Science*, *341*, 1–7.

Engelder, T. (2012), Capillary tension and imbibition sequester frack fluid in Marcellus gas shale, *Proc. Natl. Acad. Sci. U. S. A.*, *109*(52), E3625.

Feigl, K. L., et al. (1993), Space geodetic measurement of crustal deformation in central and southern California, 1984–1992, *J. Geophys. Res.*, *98*, 21,677–21,712.

Felippa, C. A., and K. C. Park (1980), Staggered transient analysis procedures for coupled mechanical systems: Formulation, *Comput. Methods Appl. Mech. Eng.*, *24*, 61–111.

Ferronato, M., G. Gambolati, C. Janna, and P. Teatini (2008), Numerical modeling of regional faults in land subsidence prediction above gas/oil reservoirs, *Int. J. Numer. Anal. Methods Geomech.*, *32*, 633–657.

Ferronato, M., N. Castelletto, and G. Gambolati (2010), A fully coupled 3-D mixed finite element model of Biot consolidation, *J. Comput. Phys.*, *229*(12), 4813–4830.

Fetkovich, M. J. (1971), A simplified approach to water influx calculations—Finite aquifer systems, *J. Pet. Technol.*, *23*, 814–828.

Fialko, Y., and M. Simons (2000), Deformation and seismicity in the Coso geothermal area, Inyo County, California: Observations and modeling using satellite radar interferometry, *J. Geophys. Res.*, *105*, 21,781–21,793.

Galloway, D. L., and T. J. Burbey (2011), Review: Regional land subsidence accompanying groundwater extraction, *Hydrogeol. J.*, *19*, 1459–1486.

Galloway, D. L., K. W. Hudnut, S. E. Ingebritsen, S. P. Phillips, G. Peltzer, F. Rogez, and P. A. Rosen (1998), Detection of aquifer system compaction and land subsidence using interferometric synthetic aperture radar, Antelope Valley, Mojave Desert, California, *Water Resour. Res.*, *34*, 2573–2585.

Gambolati, G., and R. A. Freeze (1973), Mathematical simulation of the subsidence of Venice: 1. Theory, *Water Resour. Res.*, *9*, 721–733.

Gambolati, G., P. Teatini, D. Bau, and M. Ferronato (2000), The importance of poro-elastic coupling in dynamically active aquifers of the Po river basin, Italy, *Water Resour. Res.*, *36*, 2443–2459.

Garcia, J. E. (2003), Fluid dynamics of carbon dioxide disposal into saline aquifers, PhD dissertation, Univ. of Calif., Berkeley, Calif.

Geertsma, J. (1957), The effect of fluid pressure decline on volumetric change of porous rocks, *Trans. AIME*, *210*, 331–340.

Geertsma, J. (1973), A basic theory of subsidence due to reservoir compaction: The homogeneous case, *Verhandelingen Kon. Ned. Geol. Mijnbouwk. Gen.*, *28*, 43–62.

Gens, A., I. Carol, and E. E. Alonso (1988), An interface element formulation for the analysis of soil-reinforcement interaction, *Comput. Geotech.*, *7*, 133–151.

Glowinsky, R., and P. Le Tallec (1989), *Augmented Lagrangian and Operator-Splitting Methods in Nonlinear Mechanics*, Soc. Ind. Appl. Math., Philadelphia, Pa.

Gonzalez, P. J., K. F. Tiampo, M. Palano, F. Cannavo, and J. Fernandez (2012), The 2011 Lorca earthquake slip distribution controlled by groundwater crustal unloading, *Nat. Geosci.*, *5*, 821–825.

Goodman, R. E., R. L. Taylor, and T. L. Brekke (1968), A model for the mechanics of jointed rock, *J. Soil Mech.*, *94*, 637–659.

Gray, W. G., and B. A. Schrefler (2001), Thermodynamic approach to effective stress in partially saturated porous media, *Eur. J. Mech.-A/Solids*, *20*, 521–538.

Gunasekera, D., P. Childs, J. Herring, and J. Cox (1998), A multi-point flux discretization scheme for general polyhedral grids, paper SPE 48855 presented at 6th SPE International Oil and Gas Conference and Exhibition, Society of Petroleum Engineers, Beijing, China.

Gupta, H. K. (2002), A review of recent studies of triggered earthquakes by artificial water reservoirs with special emphasis on earthquakes in Koyna, India, *Earth Sci. Rev.*, *58*, 279–310.

Hager, B. H., R. W. King, and M. H. Murray (1991), Measurement of crustal deformation using the Global Positioning System, *Annu. Rev. Earth Planet. Sci.*, *19*, 351–382.

Hanks, T. C., and H. Kanamori (1979), A moment magnitude scale, *J. Geophys. Res.*, *84*, 2348–2350.

Harris, R. A., and R. W. Simpson (1992), Changes in static stress on southern California faults after the 1992 Landers earthquake, *Nature*, *360*, 251–254.

Harris, R. A., R. W. Simpson, and P. A. Reasenberg (1995), Influence of static stress changes on earthquake locations in southern California, *Nature*, *375*, 221–224.

Howarth, R. W., R. Santoro, and A. Ingraffea (2011), Methane and the greenhouse-gas footprint of natural gas from shale formations, *Clim. Change*, *106*, 679–690.

Hubbert, M. K., and W. W. Rubey (1959), Role of fluid pressure in mechanics of overthrust faulting. I. Mechanics of fluid-filled porous solids and its application to overthrust faulting, *Geol. Soc. Am.*, *70*, 115–166.

Hughes, T. J. R. (1987), *The Finite Element Method: Linear Static and Dynamic Finite Element Analysis*, Prentice Hall, Englewood Cliffs, N. J.

IPCC (2005), *Special Report on Carbon Dioxide Capture and Storage*, edited by B. Metz et al., Cambridge Univ. Press, Cambridge, U. K.

Jackson, R. B., A. Vengosh, T. H. Darrah, N. R. Warner, A. Down, R. J. Poreda, S. G. Osborn, K. Zhao, and J. D. Karr (2013), Increased stray gas abundance in a subset of drinking water wells near Marcellus shale gas extraction, *Proc. Natl. Acad. Sci. U. S. A.*, *110*(28), 11,250–11,255.

Jaeger, J. C., and N. G. W. Cook (1979), *Fundamentals of Rock Mechanics*, Chapman and Hall, London, U. K.

Jeannin, L., M. Mainguy, R. Masson, and S. Vidal-Gilbert (2007), Accelerating the convergence of coupled geomechanical–reservoir simulations, *Int. J. Numer. Anal. Methods Geomech.*, *31*, 1163–1181.

Jha, B., and R. Juanes (2007), A locally conservative finite element framework for the simulation of coupled flow and reservoir geomechanics, *Acta Geotech.*, *2*, 139–153.

Juanes, R., J. Samper, and J. Molinero (2002), A general and efficient formulation of fractures and boundary conditions in the finite element method, *Int. J. Numer. Methods Eng.*, *54*(12), 1751–1774.

Juanes, R., E. J. Spiteri, F. M. Orr Jr., and M. J. Blunt (2006), Impact of relative permeability hysteresis on geological CO_2 storage, *Water Resour. Res.*, *42*, W12418, doi:10.1029/2005WR004806.

Juanes, R., B. H. Hager, and H. J. Herzog (2012), No geologic evidence that seismicity causes fault leakage that would render large-scale carbon capture and storage unsuccessful, *Proc. Natl. Acad. Sci. U. S. A.*, *109*(52), E3623.

Keranen, K. M., H. M. Savage, G. A. Abers, and E. S. Cochran (2013), Potentially induced earthquakes in Oklahoma, USA: Links between wastewater injection and the 2011 M_w 5.7 earthquake sequence, *Geology*, *41*, 699–702.

Khalili, N., F. Geiser, and G. E. Blight (2004), Effective stress in unsaturated soils: A review with new evidence, *Int. J. Geomech.*, *4*, 115–126.

Kim, J., H. A. Tchelepi, and R. Juanes (2011a), Stability and convergence of sequential methods for coupled flow and geomechanics: Drained and undrained splits, *Comput. Methods Appl. Mech. Eng.*, *200*, 2094–2116.

Kim, J., H. A. Tchelepi, and R. Juanes (2011b), Stability and convergence of sequential methods for coupled flow and geomechanics: Fixed-stress and fixed-strain splits, *Comput. Methods Appl. Mech. Eng.*, *200*, 1591–1606.

Kim, J., H. A. Tchelepi, and R. Juanes (2011c), Stability, accuracy and efficiency of sequential methods for coupled flow and geomechanics, *Soc. Pet. Eng. J.*, *16*(2), 249–262.

Kim, J., H. A. Tchelepi, and R. Juanes (2013), Rigorous coupling of geomechanics and multiphase flow with strong capillarity, *Soc. Pet. Eng. J.*, *18*(6), 1123–1139.

Lackner, K. S. (2003), A guide to CO_2 sequestration, *Science*, *300*(5626), 1677–1678.

LaGriT (2013), *LaGriT Manual*, Los Alamos Natl. Lab., Los Alamos, N. M.

Lei, X. Y., G. Swoboda, and G. Zenz (1995), Application of contact-friction interface element to tunnel excavation in faulted rock, *Comput. Geotech.*, *17*, 349–370.

LeVeque, R. J. (2002), *Finite Volume Methods for Hyperbolic Problems*, Cambridge Univ. Press, Cambridge, U. K.

Lewis, R. W., and B. A. Schrefler (1998), *The Finite Element Method in the Static and Dynamic Deformation and Consolidation of Porous Media*, 2nd ed., John Wiley, Chichester, U. K.

Lewis, R. W., and Y. Sukirman (1993), Finite element modelling of three-phase flow in deforming saturated oil reservoirs, *Int. J. Numer. Anal. Methods Geomech.*, *17*, 577–598.

Lewis, R. W., A. Makurat, and W. K. S. Pao (2003), Fully coupled modeling of seabed subsidence and reservoir compaction of North Sea oil fields, *Hydrogeol. J.*, *11*(1), 142–161.

Li, X., Z. Liu, and R. W. Lewis (2005), Mixed finite element method for coupled thermo-hydro-mechanical process in poro-elastic-plastic media at large strains, *Int. J. Numer. Methods Eng.*, *64*(5), 667–708.

Lofgren, B. E. (1981), Monitoring crustal deformation in The Geyser Clear Lake region, in *Research in The Geysers-Clear Lake Geothermal Area, Northern California*, p. 1141, U.S. Gov. Print. Off., Washington, D. C.

Lomeland, F., E. Ebeltoft, and T. W. Hammervold (2005), A new versatile relative permeability correlation, paper SCA 2005-32 presented at International Symposium of the Society of Core Analysts, Society of Core Analysts, Toronto, Canada.

Lomnitz, C. (1974), Earthquakes and reservoir impounding: State of the art, *Eng. Geol.*, *8*, 191–198.

Mainguy, M., and P. Longuemare (2002), Coupling fluid flow and rock mechanics: Formulations of the partial coupling between reservoir and geomechanics simulators, *Oil Gas Sci. Technol.*, *57*, 355–367.

Mandel, J. (1953), Consolidation of soils (mathematical study), *Geotechnique*, *3*, 287–299.

Marone, C. (1998), Laboratory-derived friction laws and their application to seismic faulting, *Annu. Rev. Earth Planet. Sci.*, *26*, 643–696.

McCain, W. D., Jr. (1990), *The Properties of Petroleum Fluids*, PennWell Books, Tulsa, Okla.

Minkoff, S. E., C. M. Stone, S. Bryant, M. Peszynska, and M. F. Wheeler (2003), Coupled fluid flow and geomechanical deformation modeling, *J. Pet. Sci. Eng.*, *38*, 37–56.

Molinero, J., J. Samper, and R. Juanes (2002), Numerical modeling of the transient hydrogeological response produced by tunnel construction in fractured bedrocks, *Eng. Geol.*, *64*(4), 369–386.

Morris, J. P., R. L. Detwiler, S. J. Friedman, O. Y. Vorobiev, and Y. Hao (2011a), The large-scale geomechanical and hydrogeological effects of multiple CO_2 injection sites on formation stability, *Int. J. Greenh. Gas Control*, *5*(1), 69–74.

Morris, J. P., Y. Hao, W. Foxall, and W. McNab (2011b), A study of injection-induced mechanical deformation at the In Salah CO_2 storage project, *Int. J. Greenh. Gas Control*, *5*(2), 270–280.

Mossop, A., and P. Segall (1997), Subsidence at The Geysers geothermal field, N. California from a comparison of GPS and leveling surveys, *Geophys. Res. Lett.*, *24*, 1839–1842.

Muskat, M. (1949), *Physical Principles of Oil Production*, McGraw-Hill, New York, N. Y.

Nikooee, E., G. Habibagahi, S. M. Hassanizadeh, and A. Ghahramani (2013), Effective stress in unsaturated soils: A thermodynamic approach based on the interfacial energy and hydromechanical coupling, *Transp. Porous Media*, *96*, 369–396.

Nuth, M., and L. Laloui (2008), Effective stress concept in unsaturated soils: Clarification and validation of a unified framework, *Int. J. Numer. Anal. Methods Geomech.*, *32*, 771–801.

Okada, Y. (1992), Internal deformation due to shear and tensile faults in a half-space, *Bull. Seismol. Soc. Am.*, *82*, 1018–1040.

Orr, F. M., Jr. (2009), Onshore geologic storage of CO_2, *Science*, *325*, 1656–1658.

Osborn, S. G., A. Vengosh, N. R. Warner, and R. B. Jackson (2011), Methane contamination of drinking water accompanying gas-well drilling and hydraulic fracturing, *Proc. Natl. Acad. Sci. U. S. A.*, *108*(20), 8172–8176.

Pacala, S., and R. Socolow (2004), Stability wedges: Solving the climate problem for the next 50 years with current technologies, *Science*, *305*, 968–972.

Pan, H., and H. Cao (2010), *User Manual for General Purpose Research Simulator*, Stanford Univ. Pet. Eng. Inst., Stanford, Calif.

Pao, W. K. S., and R. W. Lewis (2002), Three dimensional finite element simulation of three-phase flow in a deforming fissured reservoir, *Comput. Methods Appl. Mech. Eng.*, *191*, 2631–2659.

Park, K. C. (1983), Stabilization of partitioned solution procedure for pore fluid–soil interaction analysis, *Int. J. Numer. Methods Eng.*, *19*, 1669–1673.

Phillips, P. J., and M. F. Wheeler (2007a), A coupling of mixed and continuous Galerkin finite element methods for poroelasticity I: The continuous in time case, *Comput. Geosci.*, *11*, 131–144.

Phillips, P. J., and M. F. Wheeler (2007b), A coupling of mixed and continuous Galerkin finite element methods for poroelasticity II: The discrete-in-time case, *Comput. Geosci.*, *11*, 145–158.

Raleigh, C. B., J. H. Healy, and J. D. Bredehoeft (1976), An experiment in earthquake control at Rangely, Colorado, *Science*, *191*, 1230–1237.

Reasenberg, P. A., and R. W. Simpson (1992), Response of regional seismicity to the static stress change produced by the Loma Prieta earthquake, *Science*, *255*, 1687–1690.

Rice, J. (1992), *Fault Stress States, Pore Pressure Distributions, and the Weakness of the San Andreas Fault*, pp. 475–503, Academic Press, London, U. K.

Rice, J. R. (1993), Spatio-temporal complexity of slip on a fault, *J. Geophys. Res.*, *98*, 9885–9907.

Roeloffs, E. (1996), Poroelastic techniques in the study of earthquake-related hydrologic phenomena, *Adv. Geophys.*, *37*, 135–195.

Ruina, A. L. (1983), Slip instability and state variable friction laws, *Geophys. Res. Lett.*, *88*, 359–370.

Rutqvist, J., Y. S. Wu, C. F. Tsang, and G. Bodvarsson (2002), A modeling approach for analysis of coupled multiphase fluid flow, heat transfer, and deformation in fractured porous rock, *Int. J. Rock Mech. Min. Sci.*, *39*, 429–442.

Rutqvist, J., J. T. Birkholzer, F. Cappa, and C. F. Tsang (2007), Estimating maximum sustainable injection pressure during geological seques- tration of CO₂ using coupled fluid flow and geomechanical fault-slip analysis, *Energy Convers. Manage.*, *48*, 1798–1807.

Rutqvist, J., J. T. Birkholzer, and C. F. Tsang (2008), Coupled reservoir–geomechanical analysis of the potential for tensile and shear failure associated with CO₂ injection in multilayered reservoir–caprock systems, *Int. J. Rock Mech. Min. Sci.*, *45*, 132–143.

Rutqvist, J., D. W. Vasco, and L. Myer (2010), Coupled reservoir-geomechanical analysis of CO₂ injection and ground deformations at In Salah, Algeria, *Int. J. Greenh. Gas Control*, *4*, 225–230.

SAMG (2010), *SAMG User's Manual*, Fraunhofer Inst. for Algorithms and Sci. Comput. (SCAI), Sankt Augustin, Germany.

Samier, P., and S. Gennaro (2007), A practical iterative scheme for coupling geomechanics with reservoir simulation, paper SPE 107077 pre- sented at SPE Europec/EAGE, Society of Petroleum Engineers, London, U. K.

Schlumberger (2009), *Eclipse 100 Reference Manual 2009.1*, Schlumberger Inf. Solutions, Houston, Tex.

Scholz, C. H. (1989), Mechanics of faulting, *Annu. Rev. Earth Planet. Sci.*, *17*, 309–334.

Segall, P. (1989), Earthquakes triggered by fluid extraction, *Geology*, *17*, 942–946.

Segura, J. M., and I. Carol (2004), On zero-thickness interface elements for diffusion problems, *Int. J. Numer. Anal. Methods Geomech.*, *28*, 947–962.

Segura, J. M., and I. Carol (2008a), Coupled HM analysis using zero-thickness interface elements with double nodes. Part I: Theoretical model, *Int. J. Numer. Anal. Methods Geomech.*, *32*, 2083–2101.

Segura, J. M., and I. Carol (2008b), Coupled HM analysis using zero-thickness interface elements with double nodes. Part II: Verification and application, *Int. J. Numer. Anal. Methods Geomech.*, *32*, 2103–2123.

Settari, A., and F. Mourits (1998), A coupled reservoir and geomechanical simulation system, *Soc. Pet. Eng. J.*, *3*, 219–226.

Settari, A., and D. A. Walters (2001), Advances in coupled geomechanical and reservoir modeling with applications to reservoir compaction, *Soc. Pet. Eng. J.*, *6*, 334–342.

Sibson, R. H. (1977), Fault rocks and fault mechanisms, *J. Geol. Soc. London*, *133*, 191–213.

Sibson, R. H. (1981), Fluid flow accompanying faulting: Field evidence and models, in *Earthquake Prediction: An International Review, Mau- rice Ewing Ser.*, vol. 4, pp. 593–603, AGU, Washington, D. C.

Sibson, R. H. (1986), Brecciation processes in fault zone: Inferences from earthquake rupturing, *Pure Appl. Geophys.*, *124*, 159–175.

Sibson, R. H. (1990), Rupture nucleation on unfavorably oriented faults, *Bull. Seismol. Soc. Am.*, *80*, 1580–1604.

Sibson, R. H. (1994), Crustal stress, faulting and fluid flow, *Geol. Soc. Spec. Publ.*, *78*, 69–84.

Skempton, A. W. (1954), The pore pressure coefficients A and B, *Geotechnique*, *4*, 143–147.

Sukirman, Y., and R. W. Lewis (1993), A finite element solution of a fully coupled implicit formulation for reservoir simulation, *Int. J. Numer. Anal. Methods Geomech.*, *17*(10), 677–698.

Szulczewski, M. L., C. W. MacMinn, H. J. Herzog, and R. Juanes (2012), Lifetime of carbon capture and storage as a climate-change mitiga- tion technology, *Proc. Natl. Acad. Sci. U. S. A.*, *109*(14), 5185–5189.

Teatini, P., et al. (2011), Geomechanical response to seasonal gas storage in depleted reservoirs: A case study in the Po River basin, Italy, *J. Geophys. Res.*, *116*, F02002, doi:10.1029/2010JF001793.

Terzaghi, K., R. B. Peck, and G. Mesri (1996), *Soil Mechanics in Engineering Practice*, John Wiley, New York, N. Y.

Thomas, L. K., L. Y. Chin, R. G. Pierson, and J. E. Sylte (2003), Coupled geomechanics and reservoir simulation, *Soc. Pet. Eng. J.*, *8*(4), 350–358.

Tran, D., A. Settari, and L. Nghiem (2004), New iterative coupling between a reservoir simulator and a geomechanics module, *Soc. Pet. Eng. J.*, *9*(3), 362–369.

Tran, D., L. Nghiem, and L. Buchanan (2005), Improved iterative coupling of geomechanics with reservoir simulation, paper SPE 93244 pre- sented at SPE Reservoir Simulation Symposium, Society of Petroleum Engineers, Houston, Tex.

van der Elst, N. J., H. M. Savage, K. M. Keranen, and G. A. Abers (2013), Enhanced remote earthquake triggering at fluid-injection sites in the midwestern United States, *Science*, *341*, 164–167.

van Genuchten, M. T. (1980), A closed-form equation for predicting the hydraulic conductivity of unsaturated soils, *Soil Sci. Soc. Am.*, *44*, 892–898.

Vlahinic, I., H. M. Jennings, J. E. Andrade, and J. J. Thomas (2011), A novel and general form of effective stress in a partially saturated porous material: The influence of microstructure, *Mech. Mater.*, *43*, 25–35.

Wan, J., L. J. Durlofsky, T. J. R. Hughes, and K. Aziz (2003), Stabilized finite element methods for coupled geomechanics-reservoir flow simu- lations, paper SPE 79694 presented at SPE Reservoir Simulation Symposium, Society of Petroleum Engineers, Houston, Tex.

Wang, C. Y., L. H. Cheng, C. V. Chin, and S. B. Yu (2001), Coseismic hydrologic response of an alluvial fan to the 1999 Chi-Chi earthquake, Taiwan, *Geology*, *29*, 831–834.

Wang, H. F. (2000), *Theory of Linear Poroelasticity with Applications to Geomechanics and Hydrogeology*, Princeton Univ. Press, Princeton, N. J.

Warner, N. R., R. B. Jackson, T. H. Darrah, S. G. Osborn, A. Down, K. Zhao, A. White, and A. Vengosh (2012a), Geochemical evidence for possi- ble natural migration of Marcellus Formation brine to shallow aquifers in Pennsylvania, *Proc. Natl. Acad. Sci. U. S. A.*, *109*(30), 11,961– 11,966.

Warner, N. R., R. B. Jackson, T. H. Darrah, S. G. Osborn, A. Down, K. Zhao, A. White, and A. Vengosh (2012b), Reply to Engelder: Potential for fluid migration from the Marcellus Formation remains possible, *Proc. Natl. Acad. Sci. U. S. A.*, *109*(52), E3626.

Yerkes, R. F., and R. O. Castle (1976), Seismicity and faulting attributable to fluid extraction, *Eng. Geol.*, *10*, 151–167.

Zienkiewicz, O. C., and R. L. Taylor (2005), *The Finite Element Method for Solid and Structural Mechanics*, Elsevier, Burlington, Mass.

Zienkiewicz, O. C., D. K. Paul, and A. H. C. Chan (1988), Unconditionally stable staggered solution procedure for soil–pore fluid interaction problems, *Int. J. Numer. Methods Eng.*, *26*(5), 1039–1055.

Zoback, M. D., and S. M. Gorelick (2012a), Earthquake triggering and large-scale geologic storage of carbon dioxide, *Proc. Natl. Acad. Sci. U. S. A.*, *109*, 10,164–10,168.

Zoback, M. D., and S. M. Gorelick (2012b), Reply to Juanes et al.: Evidence that earthquake triggering could render long-term carbon stor- age unsuccessful in many regions, *Proc. Natl. Acad. Sci. U. S. A.*, *109*(52), E3624.